NUREG/CR-3980 Vol. IV
ANL-84-61 Vol. IV

NUREG/CR-3980 Vol. IV
ANL-84-61 Vol. IV

# LIGHT-WATER-REACTOR SAFETY FUEL SYSTEMS RESEARCH PROGRAMS: QUARTERLY PROGRESS REPORT

October – December 1984




ARGONNE NATIONAL LABORATORY, ARGONNE, ILLINOIS
Operated by THE UNIVERSITY OF CHICAGO

Prepared for the Office of Nuclear Regulatory Research
U. S. NUCLEAR REGULATORY COMMISSION
under Interagency Agreement DOE 40-550-75

Available from

Superintendent of Documents
U. S. Government Printing Office
Post Office Box 37082
Washington, D.C. 20013-7982

and

National Technical Information Service
Springfield, VA 22161

NUREG/CR-3980 Vol. IV
ANL-84-61 Vol. IV

Distribution
Code: R3

ARGONNE NATIONAL LABORATORY
9700 South Cass Avenue
Argonne, Illinois 60439

# LIGHT-WATER-REACTOR SAFETY FUEL SYSTEMS RESEARCH PROGRAMS: QUARTERLY PROGRESS REPORT

October--December 1984

Date Published: August 1985

Previous reports in this series

| | |
|---|---|
| ANL-83-85 Vol. IV | October--December 1983 |
| ANL-84-61 Vol. I | January--March 1984 |
| ANL-84-61 Vol. II | April--June 1984 |
| ANL-84-61 Vol. III | July--September 1984 |

Prepared for the Division of Accident Evaluation
Office of Nuclear Regulatory Research
U. S. Nuclear Regulatory Commission
Washington, D. C. 20555
Under Interagency Agreement DOE 40-550-75

NRC FIN Nos. A2016 and A2017

LIGHT-WATER-REACTOR SAFETY
FUEL SYSTEMS RESEARCH PROGRAMS
QUARTERLY PROGRESS REPORT

October-December 1984


## ABSTRACT

This progress report summarizes work performed by the Materials Science and Technology Division of Argonne National Laboratory during October, November, and December 1984 on water reactor safety problems related to fuel and cladding. The research and development areas covered are Transient Fuel Response and Fission Product Release and Clad Properties for Code Verification.


| NRC Fin No. | FIN Title |
|---|---|
| A2016 | Transient Fuel Response and Fission Product Release |
| A2017 | Clad Properties for Code Verification |

TABLE OF CONTENTS

LIGHT-WATER-REACTOR SAFETY
FUEL SYSTEMS RESEARCH PROGRAMS:
QUARTERLY PROGRESS REPORT

October-December 1984

# EXECUTIVE SUMMARY

## I. TRANSIENT FUEL RESPONSE AND FISSION PRODUCT RELEASE[a]

The theoretical FASTGRASS-VFP model has been used in the interpretation of fission gas, iodine, tellurium, and cesium release from (1) irradiated high-burnup LWR fuel in a flowing steam atmosphere during high-temperature, in-cell heating tests performed at Oak Ridge National Laboratory and (2) trace-irradiated and high-burnup LWR fuel during severe-fuel-damage (SFD) tests performed in the PBF reactor in Idaho. A theory of grain boundary sweeping of gas bubbles, gas bubble behavior during fuel liquefaction (destruction of grain boundaries due to formation of a U-rich melt phase), and U-Zr eutectic melting has been included within the FASTGRASS-VFP formalism. The grain-boundary-sweeping theory considers the interaction between the moving grain boundary and two distinct size classes of bubbles, those on grain faces and on grain edges, and provides a means of determining whether gas bubbles are caught up and moved along by a moving grain boundary or whether the grain boundary is only temporarily retarded by the bubbles and then breaks away. The theory of the effects of fuel liquefaction and U-Zr eutectic melting on fission product behavior considers the migration and coalescence of fission gas bubbles in either molten uranium, or a Zircaloy-uranium eutectic melt. Results of the analyses demonstrate that intragranular fission product behavior during both types of tests can be interpreted in terms of a grain-growth/grain-boundary-sweeping mechanism that enhances the flow of fission products from within the grains to the grain boundaries. Whereas fuel liquefaction leads to an enhanced release of

---

[a]RSR FIN Budget No. A2016; RSR Contact: L. Chan.

fission products in trace-irradiated fuel, the occurrence of fuel liquefaction in high-burnup fuel can degrade fission product release. This phenomenon is due in part to reduced gas-bubble mobilities in a viscous medium as compared to vapor transport, and in part to a degradation of grain growth rates and the subsequent decrease in grain boundary sweeping of intragranular fission products into the liquefied lamina. The analysis shows that total $UO_2$ dissolution due to eutectic melting leads to increased release for both trace-irradiated and high-burnup fuel. The FASTGRASS-VFP predictions, measured release rates from the above tests, and previously published release rates are compared and differences between fission product behavior in trace-irradiated and in high-burnup fuel are highlighted.

## II. CLAD PROPERTIES FOR CODE VERIFICATION[b]

Zircaloy fuel cladding is susceptible to local breach-type failures during power transients in LWRs because of stresses imposed by differential thermal expansion of the fuel and cladding. In this program, the effect of stress state, strain rate, and temperature on the deformation characteristics of irradiated Zircaloy fuel cladding is being investigated to provide mechanical-property information and a failure criterion for the cladding under loading conditions conducive to pellet-cladding interaction (PCI). The information will be used in the development of codes to analyze PCI in fuel rods from power ramp experiments in test reactors, and to evaluate the susceptibility of extended-burnup fuel elements and new fuel element designs in commercial reactors to PCI failures during power transients.

TEM microstructural characteristics of the H. B. Robinson Zircaloy-4 cladding tube 217A4G, which failed in a brittle manner during an expanding-mandrel test at 325°C, have been described in the previous reporting period. The microstructure of the brittle specimen was characterized by copious bulk precipitates of cubic $ZrO_2$ and hydride, <10 and 35-100 nm in size, respectively. The bulk hydride was identified in this reporting period to be fcc $\delta$ hydride. The characteristic structures containing the cubic-$ZrO_2$ and $\delta$-hydride precipitates were also observed in Zircaloy-2 cladding specimens

[b]RSR FIN Budget No. A2017; RSR Contact: H. H. Scott.

165AG10 and 165AE4B from the Big Rock Point Reactor, which failed in a brittle manner during internal gas-pressurization tests. Stereopairs of weak-beam dark-field images were analyzed to show the bulk nature of the cubic-$ZrO_2$ and δ-hydride precipitates by the "$2\frac{1}{2}$D-microscopy" technique.

Some TEM thin-foil specimens from tubes that exhibited brittle-fracture behavior were irradiated with 1-MeV electrons in the HVEM at 325°C in a vacuum of ~$1.3 \times 10^{-4}$ Pa. The in-situ irradiation experiment showed that radiation-induced precipitation of $Zr_3O$ and cubic $ZrO_2$ occurs at 325°C in the specimens. However, neither precipitation nor dissolution of the δ hydride was observed during the HVEM irradiation; thus, the δ hydride presumably forms by thermal aging.

Several Zircaloy cladding sections and metallographic specimens that contain actual PCI defects produced during operation of a commercial power reactor were obtained. A microstructural evaluation of these specimens will be performed to identify the phases present in the material for comparison with results obtained on irradiated material that exhibited brittle-fracture behavior in the internal gas-pressurization and mandrel-loading experiments.

# I. TRANSIENT FUEL RESPONSE AND FISSION PRODUCT RELEASE

Principal Investigator:
J. Rest

## A. Grain Boundary Sweeping and Liquefaction-induced Fission Product Behavior in Nuclear Fuel Under Severe Core Damage Accident Conditions

(J. Rest and S. A. Zawadzki)

### 1. FASTGRASS-VFP Model for Grain-Growth/Grain-Boundary-Sweeping

FASTGRASS-VFP[1-3] is a mechanistic computer model for predicting the behavior of fission gas and volatile fission products (VFPs) in solid $UO_2$-based fuels during steady-state and transient conditions. The model accounts for the effects of a number of processes on both the distribution of fission products within the fuel and the amount released. These processes include fission product generation; gas bubble nucleation and re-solution; bubble migration and coalescence; interaction between I, Cs, CsI, and fission gas bubbles; chemical reaction between I, Cs, and fuel; channel formation on grain faces; interlinked porosity on grain edges; and microcracking. The present version of the theory models the fission gases Xe and Kr; the volatiles I, Cs, Te; and the major VFP reaction products, CsI, $Cs_2MoO_4$, and $Cs_2UO_4$. Including the latter two reaction products can alter the Cs and CsI release predictions by up to 10%.[2] Fission products released from the fuel are assumed to reach the pellet surface by successively migrating from the grain interiors to grain faces and then to the grain edges, with subsequent transport through a network of interconnected tunnels and as-fabricated porosity.

FASTGRASS-VFP has recently been used[4,5] in the interpretation of fission gas, iodine, cesium and tellurium release from irradiated high-burnup LWR fuel in a flowing steam atmosphere during high-temperature, in-cell heating tests performed at Oak Ridge National Laboratory (ORNL), and trace-irradiated and high-burnup LWR fuel during severe-fuel-damage (SFD) tests performed in the PBF Reactor in Idaho. The results of these analyses demonstrated that intragranular fission product behavior during both types of tests can be interpreted in terms of a grain-growth/grain-boundary-

sweeping mechanism that enhances the flow of fission products from within the grains to the grain boundaries. Basically, the model assumes that small intragranular bubbles (consisting, in general, of Xe, Kr, I, Cs, and CsI), and gaseous and VFP atoms in the path of a growing grain, are swept up by grain boundary adhesive forces. Such grain boundary sweeping provides another mechanism for the collection of fission products at grain faces and edges.

The FASTGRASS-VFP theory[5] of grain boundary sweeping of gas bubbles considers the interaction between the moving grain boundary and two distinct size classes of bubbles, those on grain faces and on grain edges, and provides a means of determining whether gas bubbles are caught up and moved along by a moving grain boundary or whether the grain boundary is only temporarily retarded by the bubbles and then breaks away.

Speight and Greenwood[6] proposed a grain growth theory which includes the sweeping of entrapped microbubbles by the front of an advancing grain boundary. The basic postulate of their theory is that small bubbles exert a minimal drag force on an advancing grain surface and thus are swept along with the moving boundary, while large bubbles detach from the advancing surface because of their higher drag. To assess the efficiency of bubble sweeping, they compared the magnitude of the force exerted by a bubble on the boundary, i.e.,

$$F_b = \pi R_b \gamma_{gb} \sin 2\phi \quad , \tag{1.1}$$

with the adhesive effects of the interfacial surface tension, i.e.,

$$F_{gb} = \frac{2\gamma_{gb}}{r_c} \pi r_{gb}^2 \quad , \tag{1.2}$$

where $R_b$ = bubble radius, $\gamma_{gb}$ = grain boundary surface tension, $\phi$ = angle of contact between the bubble and the boundary, $r_c$ = radius of curvature of the grain, and $2r_{gb}$ = characteristic distance of bubble spacing.

Whereas Speight and Greenwood considered the effects of the moving boundary interacting with a population of equal-sized bubbles, the present

theory includes the effects on the moving boundary of two distinct distributions of bubble sizes, those on the grain faces and those on the grain edges: the motion of the moving boundary is retarded by the presence of both grain face and grain edge bubbles. In addition, as FASTGRASS-VFP provides for a mechanistic calculation of intra- and intergranular fission product behavior, the coupled calculation between fission gas behavior and grain growth is kinetically comprehensive. The magnitude of the total force exerted by the bubbles on the boundary, or vice versa, depends on bubble radius and angle of contact according to the relationship

$$F_b = \pi R_f N_f \gamma_{gb} \sin 2\phi_f + \pi R_e N_e \gamma_{gb} \sin 2\phi_e \equiv N_f F_f + N_e F_e, \qquad (1.3)$$

where the subscripts f and e denote grain face and grain edge bubbles, respectively; $R_f$ and $R_e$ are the corresponding bubble radii; $N_f$ and $N_e$ are the corresponding numbers of bubbles; $\phi_f$ and $\phi_e$ are the corresponding angles of contact between the bubbles and the boundary; and $F_f$ and $F_e$ represent, respectively, the forces exerted by a grain face and grain edge bubble on the boundary.

The velocity of these bubbles can be determined from the individual forces on the bubbles by utilizing the Nernst-Einstein equation. Assuming that the grain face and grain edge bubbles move by surface diffusion control, the velocity of these bubbles can be expressed as

$$V_f = \frac{D_f F_f}{kT} = \frac{3}{4} \frac{a_o^4 D_o}{R_f^3} \left(\frac{2\gamma_{gb}}{kT}\right) \sin 2\phi_f \exp\left(\frac{-E_s}{kT}\right) \qquad (1.4)$$

and

$$V_e = \frac{D_e F_e}{kT} = \frac{3}{4} \frac{a_o^4 D_o}{R_e^3} \left(\frac{2\gamma_{gb}}{kT}\right) \sin 2\phi_e \exp\left(\frac{-E_s}{kT}\right), \qquad (1.5)$$

where $V_f$ and $V_e$, and $D_f$ and $D_e$ are the velocities and diffusion coefficients of the face and edge bubbles, respectively, k is Boltzmann's constant, T is the absolute temperature, $a_o$ is the lattice constant, $D_o$ is the preexponential factor for surface self-diffusion of the matrix solid, and $E_s$ is the activation energy for this process.

In order to determine the contact angles $\phi_f$ and $\phi_e$ in Eqs. (1.4) and (1.5), the velocity of the moving grain boundary needs to be evaluated. At temperatures of about 1900 K, atomic mobilities in $UO_2$ result in an enhanced migration of atoms from the convex to the concave side of a curved boundary. The atoms move toward the concave side of the boundary because in that location, they are surrounded by a somewhat larger number of neighboring atoms and thereby exhibit a lower effective energy state. In other words, the net flux of atoms, J, across a curved grain boundary occurs because the binding energy of the atoms in the matrix is somewhat higher on the concave than on the convex side of the boundary. The net result of this atomic motion is shrinkage of small grains with predominantly convex surfaces and growth of larger grains with concave surfaces. The net flux of atoms across the boundary can be expressed as[7]

$$J = \frac{\nu}{a_o^2} \frac{\Delta E}{kT} \exp(-Q/kT), \tag{1.6}$$

where $\nu$ is the frequency of vibration of an atom in the solid lattice adjacent to the boundary, $\Delta E$ is the difference in energy between two atoms located on opposite sides of the boundary, and Q is the activation energy for grain boundary motion. The velocity of the grain boundary, $V_{gb}$, is the product of the flux J and the atomic volume, which is approximately equal to the cube of the lattice constant:

$$V_{gb} = Ja_o^3 = \nu a_o \frac{\Delta E}{kT} \exp(-Q/kT). \tag{1.7}$$

The energy difference $\Delta E$ can be related to the intrinsic properties of the curved grain boundary and to the sizes and numbers of gas bubbles attached to the boundary. In the absence of differential strain between adjacent grains, the intrinsic grain-boundary tension force is the primary force acting on the boundary, and acts to move the boundary toward the center of curvature of the convex grain. The grain face and grain edge bubbles exert a drag force in the opposite direction. If a section of grain boundary with area $A_{gb}$ moves a distance dx, then

$$\Delta E = \left[ \frac{2\gamma_{gb}}{r_c} (A_{gb}) - F_b \right] dx, \tag{1.8}$$

where $F_b$ is given by Eq. (1.3). The first term in the brackets in Eq. (1.8) represents the adhesive effects of the interfacial surface tension, i.e., $F_{gb}$ of Eq. (1.2). The number of atoms displaced from one side of the boundary to the other is

$$\frac{A_{gb}\,dx}{a_o^3} .$$

Dividing this expression into the preceding one gives the energy change per atom transferred across the boundary, $\Delta E$:

$$\Delta E = \frac{2a_o^3\gamma_{gb}}{r_c}\left(1 - \frac{\pi R_f N_f r_c \sin 2\phi_f}{2A_{gb}} - \frac{\pi R_e N_e r_c \sin 2\phi_e}{2A_{gb}}\right). \qquad (1.9)$$

Inserting Eq. (1.9) into Eq. (1.7) yields the grain boundary velocity

$$V_{gb} = \frac{2a_o^4\,\nu\gamma_{gb}}{r_c kT}\exp(-Q/kT)\left[1 - 1/2\left(\frac{\pi N_f R_f^2}{A_{gb}}\right)\left(\frac{r_c}{R_f}\right)\sin 2\phi_f - 1/2\left(\frac{\pi N_e R_e^2}{A_{gb}}\right)\left(\frac{r_c}{R_e}\right)\sin 2\phi_e\right] . \qquad (1.10)$$

When the bubbles are widely spaced or very small, the second and third terms in the brackets in Eq. (1.10) are negligible compared to unity, and $V_{gb}$ reduces to the intrinsic velocity of the curved grain boundary. The second and third terms in the brackets in Eq. (1.10) account for the retarding effects of the bubbles on grain boundary motion.

If both the grain face and grain edge bubbles are swept along with the moving boundary, then

$$V_f = V_e = V_{gb} . \qquad (1.11)$$

The first equality in Eq. (1.11) yields

$$\frac{\sin 2\phi_f}{R_f^3} = \frac{\sin 2\phi_e}{R_e^3} . \qquad (1.12)$$

From Eqs. (1.10-1.12), one obtains

$$\sin 2\phi_e = \left[ \frac{3}{4} \frac{D_o r_c}{R_e^3 \nu} \exp\left( - \frac{E_s - Q}{kT} \right) + 1/2 \left( \frac{\pi N_e R_e^2}{A_{gb}} \right) \left( \frac{r_c}{R_e} \right) + 1/2 \left( \frac{\pi N_f R_f^2}{A_{gb}} \right) \left( \frac{r_c}{R_f} \right) \left( \frac{R_f}{R_e} \right)^3 \right]^{-1} . \quad (1.13)$$

Since sin $2\phi$ cannot exceed unity, the condition for bubble detachment is met when the right-hand side of Eq. (1.13) exceeds unity. If this condition is satisfied and $R_f = R_e$, both face and edge bubbles become detached from the boundary. If $R_f \neq R_e$, the larger bubble becomes detached (we assume for the sake of this discussion that $R_e > R_f$) and the condition that the smaller bubble be swept along with the moving boundary is examined by requiring

$$V_f = V_{gb},$$

which results in

$$\sin 2\phi_f = \left[ \frac{3}{4} \frac{D_o r_c}{R_f^3 \nu} \exp\left( - \frac{E_s - Q}{kT} \right) + 1/2 \left( \frac{\pi N_f R_f^2}{A_{gb}} \right) \left( \frac{r_c}{R_f} \right) \right]^{-1} . \quad (1.14)$$

If the right-hand side of Eq. (1.14) exceeds unity, then the smaller bubble ($R_f$ in this case) is also detached from the boundary. If the right-hand side of Eq. (1.13) or (1.14) is less than unity, both face and edge bubbles, or just face bubbles, respectively, are swept along with the moving boundary. The contact angles $\phi_f$ and $\phi_e$ can be computed from Eqs. (1.12-1.14) and used in Eqs. (1.4) and (1.5) or (1.10) to determine the bubble or grain boundary velocity.

Fuel stoichiometry can have a pronounced effect on atomic mobilities in $UO_2$ fuel and thus on grain growth kinetics. Data[8] on the diffusivity of $^{133}Xe$ in $UO_{2+x}$ as a function of fuel stoichiometric condition show that increased levels of oxygen in solution in $UO_2$ lead to observed increases in the diffusivity of $^{133}Xe$ and $^{85}Kr$. For example, a change from $UO_{2.0}$ to $UO_{2.12}$ can increase the diffusivity of $^{133}Xe$ by more than two orders of magnitude. Thus, the stoichiometry of the oxide can have a significant impact on atomic mobility and grain growth characteristics. Indeed,

for the highly oxidizing environment of fuel exposed to steam flow at elevated temperatures, $UO_2$ can be expected to become hyperstoichiometric ($0 < x \leq 0.15$) during the course of a severe-core-damage accident.[9]

To account for such oxidation effects, two values of the activation energy, Q, are employed in the present version of FASTGRASS-VFP. For stoichiometric $UO_{2.00}$ (nominal grain growth), Q = 357 kJ/mole. This value of Q for stoichiometric fuel is close to the value of 360 kJ/M determined by MacEwan and Hayashi.[10] For hyperstoichiometric (oxidized) fuel, the activation energy is decreased to Q = 294 kJ/Mole, approximately proportional to the difference in activation energy between $UO_2$ and $UO_{2+x}$ reported by Turnbull.[11] This value of Q, for oxidized $UO_2$, was determined by the requirement that the integrated intragranular Xe release as calculated by FASTGRASS-VFP must be consistent with measured total (end-of-test) release values for SFD-ST.

As the boundary moves, the rate $\frac{dC_{gb}}{dt}$ at which fission products are swept up by the moving boundary is proportional to the rate of change of the volume of the grain; i.e.,

$$\frac{dC_{gb}}{dt} = \frac{\pi e C_I D_t^2}{2} \frac{dD_t}{dt} = \frac{\pi e C_I D_t^2 V_{gb}}{2} , \qquad (1.15)$$

where $C_I$ is the intragranular concentration of a fission product, $D_t$ is the grain diameter at time t, and e is a factor that describes the grain boundary sweeping efficiency. The value of e is assumed to be unity for the fission gases, I, and CsI (in bubbles), and 0.6 for atomic Cs. The lower value of e for Cs is consistent with the high chemical affinity of Cs for $UO_2$, other fission products, and metallic inclusions.

For each fission product, Eq. (1.14) provides one term in the overall equations for the various $dC_I/dt$ and one term in the overall equations for the various intergranular fission products, $dC_B/dt$ (e.g., see Ref. 3). The bubble radii, the intra- and intergranular concentrations of the fission products, the grain size, and the fraction of the grain boundary area occupied by bubbles ($\pi N_f R_f^2/A_{gb}$ and $\pi N_e R_e^2/A_{gb}$ in Eqs. 1.10, 1.13 and

1.14) are calculated as a function of time. The values employed for various quantities used in Eqs. (1.4-1.5) and (1.10-1.14) are $\nu = 1.0 \times 10^{12}$ $s^{-1}$, $r_c = D_t/2$, $D_o = 4 \times 10^5$ $cm^2/s$, and $E_s = 453.6$ kJ/mole.

## 2. FASTGRASS-VFP Model for the Behavior of Fission Products During Fuel Liquefaction and Dissolution

A wide range of material interaction and phase transformation phenomena can be expected at the elevated temperatures associated with severe core damage accidents; one of the more significant is the steam-cladding (Zircaloy) reaction, with $ZrO_2$ and oxygen-stabilized alpha-Zircaloy [$\alpha$-Zr(O)] byproducts. The formation of partially oxidized Zircaloy species in turn can result in the reduction of the $UO_2$ fuel and the formation of a U-Zr-O ternary phase system (liquefaction), with a pronounced alteration in thermal, chemical, and physical properties. Significant cladding-fuel interaction can result in U-Zr eutectic melting of fuel (if the eutectic melting temperature is attained) and the attendant potential for enhanced fission product release from the melt.

The results of recent experiments[12,13] indicate that molten $\alpha$-Zr(O) dissolution of $UO_2$ fuel is initially controlled by wetting characteristics, where reduction of $UO_2$ to a hypostoichiometric ($UO_{2-x}$) condition is a prerequisite to fuel dissolution. The experiments indicated that the initial kinetics of dissolution were not affected by grain size. It was observed that molten Zircaloy first penetrated $UO_2$ only along gross macrocracks, rather than at grain boundaries. However, once the dissolution process commenced, liquid uranium ($T_{mp}$ = 1405 K) apparently precipitates preferentially along the $UO_{2-x}$ grain interfaces. The formation of the low-melting-point U-rich phase apparently results in loss of grain boundary cohesion of the polycrystalline fuel and appears responsible for sudden fuel dissolution, resulting in the dispersion of grain-size particles in a U/Zr-melt phase. As discussed by the authors,[12,13] the extent of such grain boundary dissolution is controlled not only by contact duration and temperature, but also by the total mass of the $UO_2$/Zr system, the initial porosity of the $UO_2$ sample, and the oxidation state of Zr.

A model describing the behavior of fission gases and volatile fission products during fuel liquefaction and dissolution has been developed and incorporated into FASTGRASS-VFP. Fuel liquefaction is defined to be the destruction of the $UO_2$ grain boundaries at fuel temperatures in excess of 2170 K via reduction of the $UO_{2.0}$ to $UO_{2-x}$ with the subsequent precipitation of a U-rich melt phase along the boundaries. Under these conditions, release of fission products occurs primarily by fission product migration through the liquefied U, or U-Zr lamina (or film), to the fuel surface. Melting of U-Zr eutectic occurs at fuel temperatures in excess of 2650 K and results in gross dissolution of the fuel grains. Fission product release under eutectic melt conditions occurs by fission product migration through the melt to a free surface. Gas bubble mobility in the U/U-Zr melt can occur via bubble rise in a viscous liquid, evaporation-condensation, and volume diffusion.

Escape of gas bubbles from the fuel during liquefaction conditions, in the absence of strong temperature gradients, is due primarily to the motion of relatively large bubbles under the action of the gravitational force, through the liquefied lamina, to the surface of the fuel (the lamina is assumed to be 1-2 μm thick, and exists along the destroyed grain boundaries). This is in contrast to release processes in solid fuel, where release can occur directly upon the arrival of fission gas at the grain edges if a stable network of interconnected porosity is encountered.

Modeling of bubble rise in a viscous liquid is based on an estimate of the pore rise time from the interior of the melt to the free surface. An approximation of the bubble velocity can be obtained by assuming that bubble interference during an increment of time is negligible and variations in properties along the distance of travel are minimal. Under such assumptions, the classical expression for bubble rise in a viscous liquid can be employed. If a submerged, rigid bubble is allowed to rise from rest in the liquid, it will accelerate until it reaches a constant terminal velocity ($V_t$). At this condition, the effects of gravity ($F_g$) and drag ($F_d$) are just balanced by that due to buoyancy ($F_b$); i.e., the equilibrium force balance for such steady-state bubble rise can be written as

$$\frac{4}{3}\pi R_b^3 \rho_L g = \frac{4}{3}\pi R_b^3 \rho_g g + 6\pi R_b \mu_L (V_t), \quad (1.16)$$

where

$R_b$ = bubble radius,
$\rho_L$ = liquid fuel density,
$g$ = gravitational constant,
$\rho_g$ = bubble gas density, and
$\mu_L$ = viscosity of liquefied fuel.

Noting that $\rho_L >> \rho_g$, one can express the terminal rise velocity as

$$V_t = \frac{2 R_b^2 \rho_L g}{9\mu_L}. \quad (1.17)$$

Fission gas bubbles can also migrate in the liquid via a volume diffusion mechanism. The diffusivity of a bubble of radius $R_b$ migrating by volume diffusion is

$$D_b = \frac{3\Omega}{4\pi R^3} D_u, \quad (1.18)$$

where $\Omega$ is the molecular volume and $D_u$ is the U-atom diffusivity.

The U-atom diffusivity, $D_u$, in molten $UO_2$ is based on the Sutherland-Einstein model and is given by[14]

$$D_u = \frac{kT}{4\pi r_a \mu_L}. \quad (1.19)$$

The parameter values used in Eq. (1.19) are

$k = 1.38(10^{-16})$ erg/K $= 1.28(10^{-16})$ g·cm$^2$/s$^2$·K,
$\mu_L$ = $UO_2$ liquid viscosity $= 4(10^{-2})$ g/s·cm,
$r_a$ = U-atomic radius $= 1.42(10^{-8})$ cm,

$\frac{k}{4\pi r_a \mu_L} = 1.93(10^{-8})$ cm$^2$/s·K, and

$T$ = liquid $UO_2$/$\alpha$-Zr(O) temperature.

From Eq. (1.19) with the above parameter values, $D_u = 4.15 \times 10^{-5}$ $cm^2/s$ at T = 2200 K. This is to be compared with a xenon diffusivity in solid fuel of $2 \times 10^{-13}$ $cm^2/s$ based on an extrapolation of Cornell's data.[15]

FASTGRASS-VFP analyses of the PBF SFD 1-1 test (e.g., see Section 6) indicate that significant liquefaction-induced release during the test depends on the initial coalescence and growth of relatively small (~0.04 μm) diameter bubbles in the liquefied material due to a volume diffusion mechanism. Whereas volume diffusion (i.e., self diffusion of the $U^{4+}$ ion) is relatively slow in solid $UO_2$, it appears to be a significant factor in the motion of small bubbles in liquefied $UO_2$. The growth of small bubbles in the liquefied material is predicted to occur mainly by the volume diffusion mechanism until the bubbles reach sufficient size such that their mobility by viscous flow is high enough to promote appreciable bubble sweep-up. Subsequently, the release of fission gas (and other fission products trapped in the bubbles) is dominated by the motion of relatively large bubbles (~1 μm diameter) under buoyant forces. If a relatively large temperature gradient exists in the material, the bubbles can attain an appreciable mobility via the evaporation-condensation mechanism. However, as the tests discussed in this paper had relatively small temperature gradients, the evaporation-condensation mechanism will not provide competitive mobilities when compared to viscous flow.

### 3. Fission Product Behavior in High-Burnup Fuel During ORNL In-Cell Heating Tests with No Fuel Liquefaction

Figures 1.1 and 1.2 show FASTGRASS-VFP predictions of fission gas and Cs release for ORNL tests HI-1 and HI-3,[16] and compare them with the corresponding measured quantities. The effects of fuel liquefaction are not considered here, but will be discussed in Section 4. Tests HI-1 and HI-3 were conducted for 30 min at 1673 K and 20 min at 2273 ± 50 K, respectively, within a flowing steam environment. The fuel specimens were 20-cm-long sections of H. B. Robinson fuel rod irradiated to 28,000 MWd/MTU. In order to assess correctly the state of the fuel prior to the test, a thermally and mechanically coupled model consisting of FASTGRASS-VFP and the LIFE-LWR fuel behavior code was used for the in-reactor irradiation period.[3] The total gas released during the irradiation was about 0.2%.

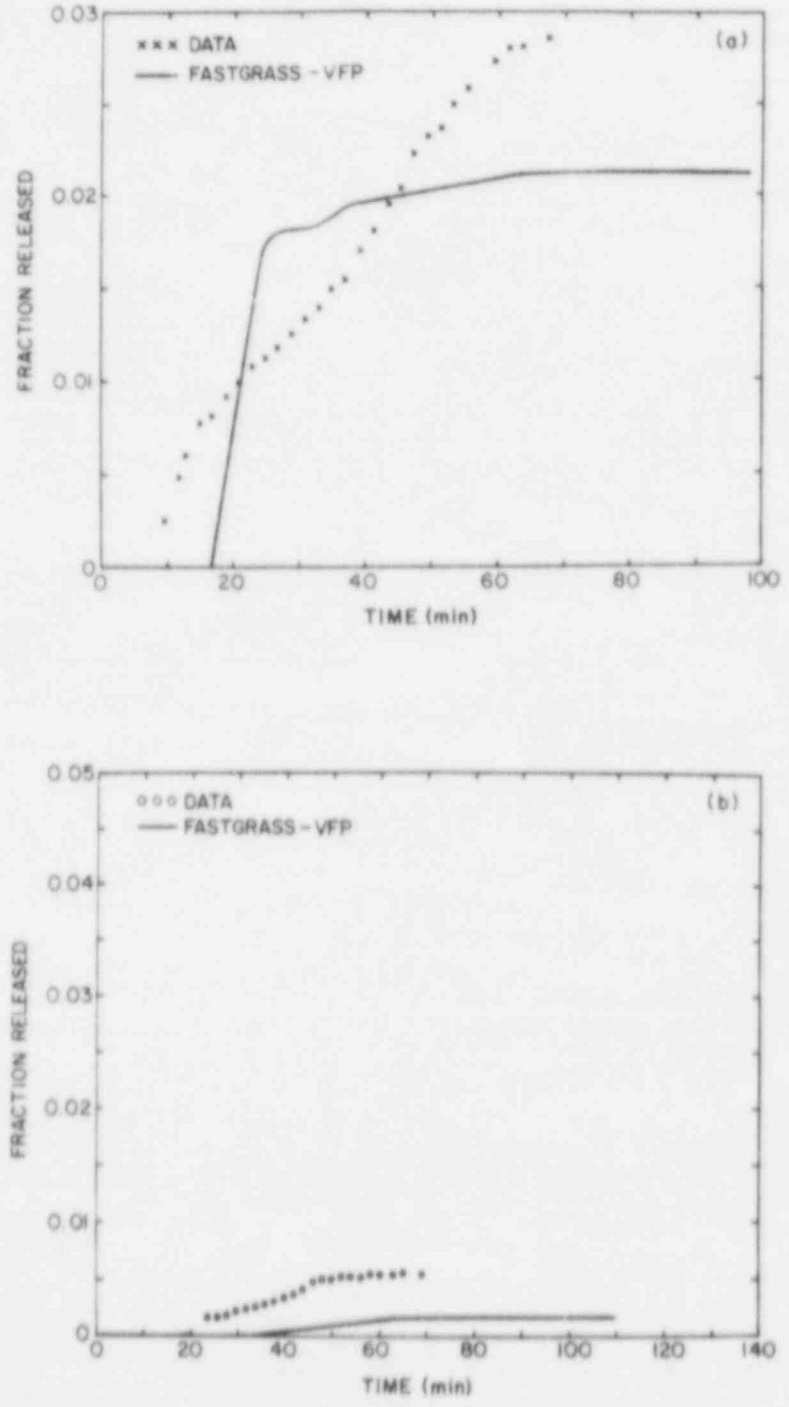


Fig. 1.1. FASTGRASS-VFP Predictions of (a) Fission Gas and (b) Cesium Release During ORNL Test HI-1, Compared with Measured Values.

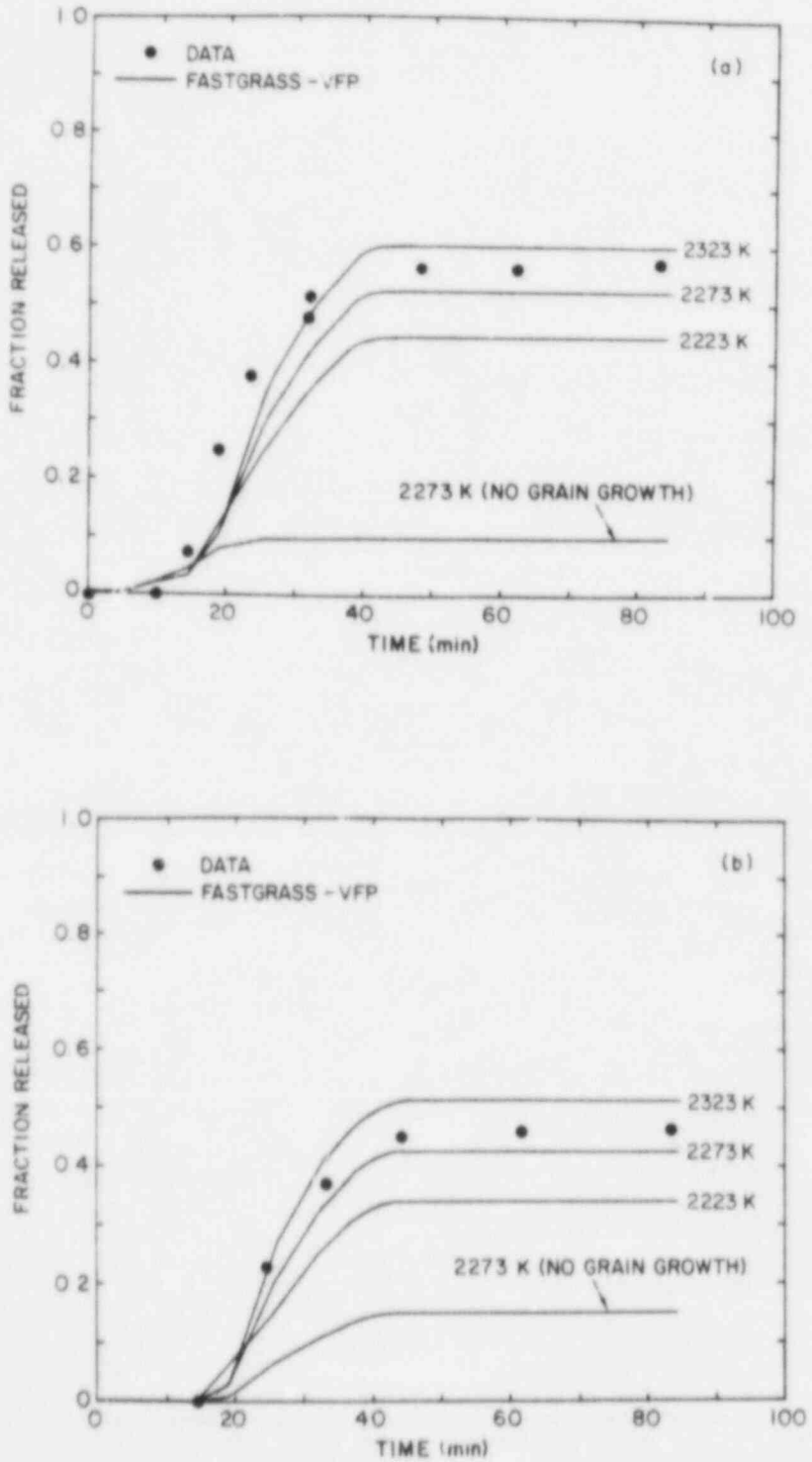


Fig. 1.2. FASTGRASS-VFP Predictions of (a) Fission Gas and (b) Cesium Release During ORNL Test HI-3, Compared with Measured Values.

The value of Q for stoichiometric $UO_{2.00}$ was used for both test simulations: This resulted in predictions of no grain growth for HI-1 and a 26-45% increase in grain size for HI-3. These grain growth predictions are consistent with microscopic observations. Figure 1.3 shows scanning electron micrographs of H. B. Robinson fuel specimens before and after test HI-3; the grain size before transient heating was approximately 4.2 μm, whereas post-test examination indicates an ~50% increase in grain size. More detailed microscopic results are presented in Ref. 17.

In order to reflect the reported experimental uncertainty in temperature for test HI-3, each part of Fig. 1.2 includes three predicted curves, which correspond to test temperatures of 2273 ± 50 K. Also shown in Fig. 1.2 are the predictions of the theory in the absence of grain growth. On the basis of the reasonable agreement between theory and data for fission gas and Cs release when a grain-growth/grain-boundary-sweeping mechanism is operative (Fig. 1.2), and the agreement between predicted and observed end-of-test grain size, it is concluded that grain boundary sweeping of fission products is a key mechanism for moving fission products from within the grains to the grain boundaries under HI-3 test conditions.

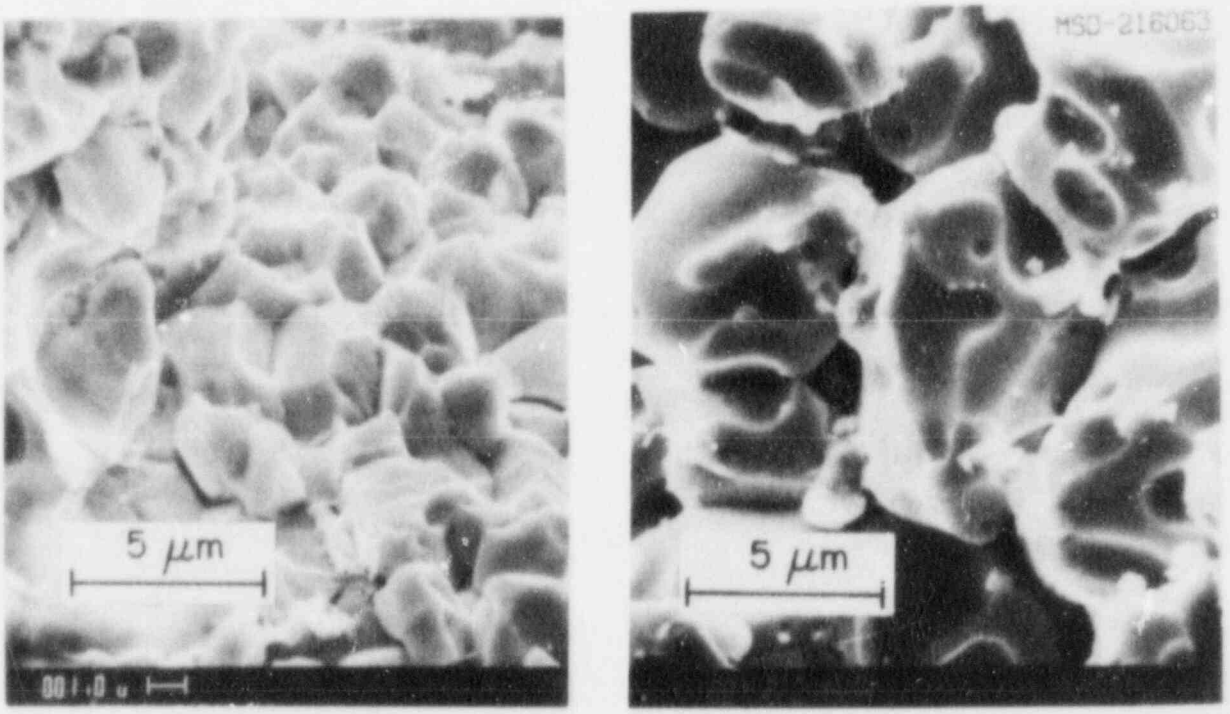


Fig. 1.3. Scanning Electron Micrographs of H. B. Robinson Fuel (Left) Before and (Right) After ORNL Test HI-3.

It should be noted that whereas partial oxidation of the cladding was observed after tests HI-3, no visual evidence of appreciable fuel oxidation was detected.[17] This result is consistent with the use of the stoichiometric grain growth law within FASTGRASS-VFP for HI-1, HI-3, and HI-4 (see Section 4) test conditions.

Figure 1.4 shows FASTGRASS-VFP predictions of fission gas and Cs release for test HI-2.[16] The HI-2 test specimen was similar to those used in tests HI-I and HI-3. Test HI-2 was conducted for 20 min at about 1973 K in flowing steam. Metallographic examination[16,17] of the tested fuel specimen revealed extensive fractures in the cladding, essentially complete oxidation to $ZrO_2$, and evidence of fuel-cladding interaction. Thus, it seems likely that fuel oxidation did occur during test HI-2, in contrast to tests HI-1, HI-3, and HI-4. Each part of Fig. 1.4 shows predicted curves obtained with both the stoichiometric ("nominal") grain growth activation energy (maximum fuel temperature = 1973 K) and the hyperstoichiometric ("enhanced") grain growth activation energy (maximum fuel temperature = 1973 ± 50 K), as well as the predictions of the theory for the case of no grain growth (maximum fuel temperature = 1973 K). For the cases where the hyperstoichiometric grain growth activation energy is used, there is reasonable agreement between theory and experiment. Thus, both the experimental results available to date and the FASTGRASS-VFP analyses (Fig. 1.4) indicate that the $UO_2$ diffusivities were enhanced to some extent during test HI-2 owing to $UO_2$ oxidation to $UO_{2+x}$.

### 4. Fission Product Behavior in High-Burnup Fuel During ORNL In-Cell Heating Tests with Fuel Liquefaction

Figure 1.5 shows FASTGRASS-VFP predictions of fission gas release for test HI-3 with and without the effects of fuel liquefaction, compared with the experimental observations. As discussed in Section C and shown in Figs. 1.2 and 1.5 (dashed curve), the FASTGRASS-VFP calculations made with the assumption of no liquefaction are in good agreement with the data. The calculations made with the assumption that fuel liquefaction occurred in test HI-3 (solid curve in Fig. 1.5) show a degradation in the fission gas

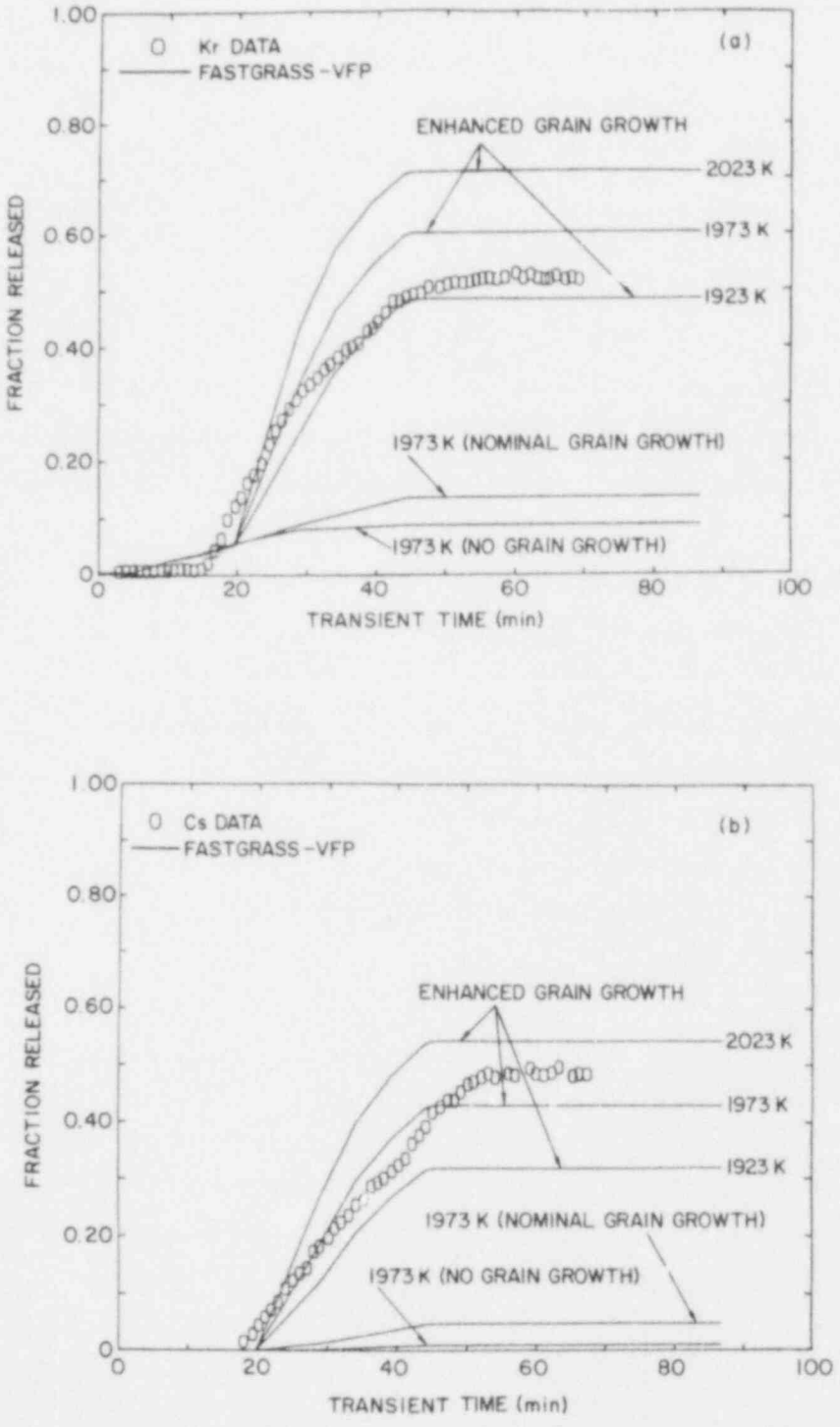


Fig. 1.4. FASTGRASS-VFP Predictions of (a) Fission Gas and (b) Cesium Release During ORNL Test HI-2, Compared with Measured Values.

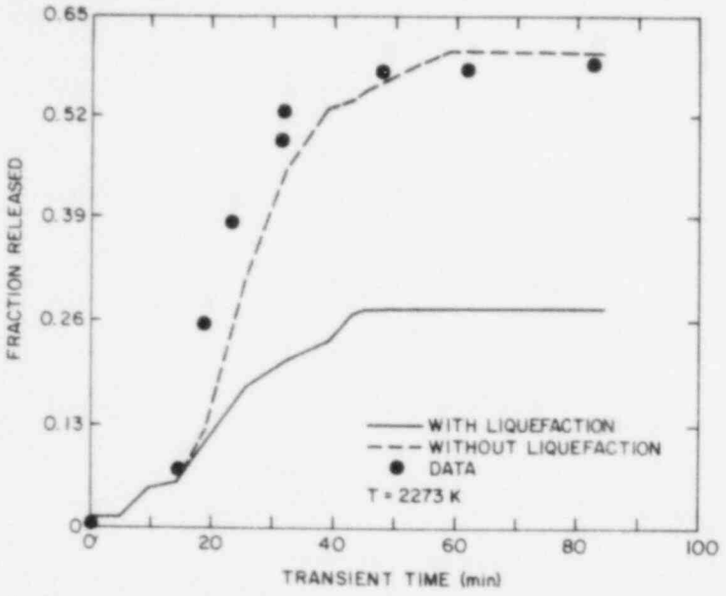


Fig. 1.5

FASTGRASS-VFP Predictions of Fission Gas Release During ORNL Test HI-3 (Max. Fuel Temperature = 2273 K) With and Without the Effects of Fuel Liquefaction, Compared with Measured Values.

release, and are not in agreement with the data. The reason for this result is that during fuel liquefaction, the resultant enhanced growth of fission gas bubbles in the liquefied lamina bordering the $UO_2$ grains reduces grain growth rates and reduces grain boundary sweeping of intragranular fission products into the liquefied region. In addition, just subsequent to fuel liquefaction, fission product release rates are reduced owing to decreased mobility in a viscous medium as compared to vapor transport through interconnected tunnels. The effect of reduced grain growth rates during fuel liquefaction is demonstrated in Fig. 1.6, which shows FASTGRASS-VFP predictions for grain growth during test HI-3 with and without the effects of fuel liquefaction. Also shown in Fig. 1.6 is the reported grain size observed in the post-tested fuel. As shown in Fig. 1.6, the predicted grain size without the effects of fuel liquefaction is consistent with the observations, whereas the calculated grain size for the case of fuel liquefaction is substantially below the reported values. The FASTGRASS-VFP results for fission gas release and grain growth during test HI-3 in the absence of any fuel liquefaction are consistent with the result that only minimal evidence of fuel liquefaction was observed in test HI-3.[18]

Figure 1.7 shows FASTGRASS-VFP results for fission gas release during test HI-4 with and without the effects of fuel liquefaction, compared to the experimental observations. The fuel specimen for test HI-4[16]

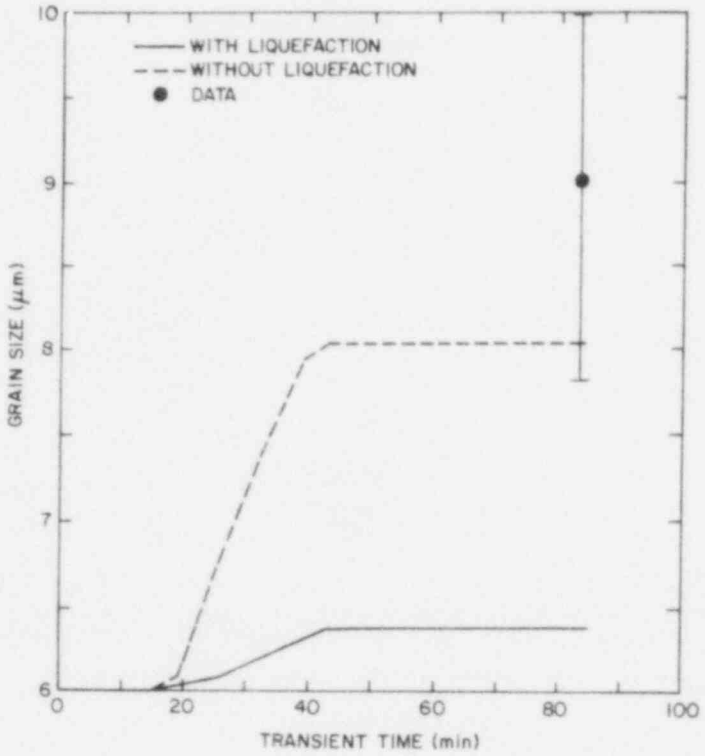


Fig. 1.6. FASTGRASS-VFP Predictions of Grain Growth During ORNL Test HI-3 With and Without the Effects of Fuel Liquefaction, Compared with Measured Values.

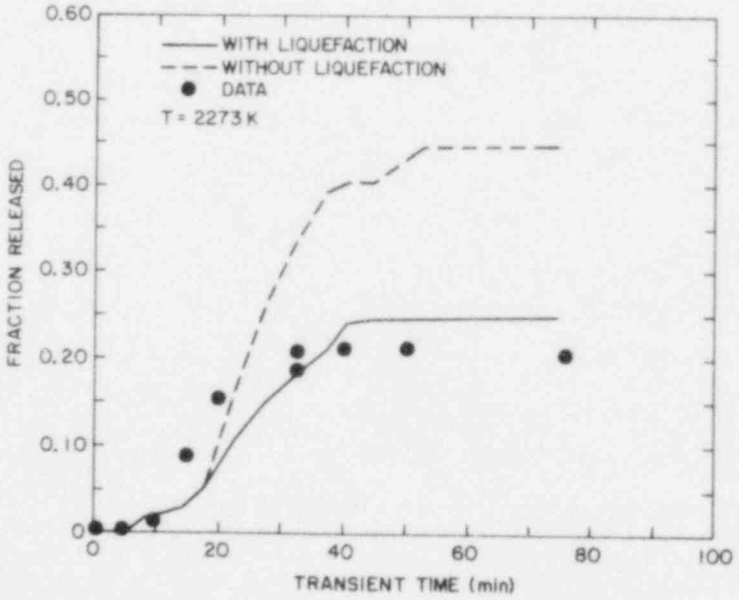


Fig. 1.7. FASTGRASS-VFP Predictions of Fission Gas Release During ORNL Test HI-4 (Max. Fuel Temperature = 2273 K) With and Without the Effects of Fuel Liquefaction, Compared with Measured Values.

consisted of a 20.3-cm-long fuel segment from a rod which had been irradiated in the Peach Bottom-2 reactor to about 10,100 MWd/MTU. Again, FASTGRASS-VFP/LIFE-LWR was used to simulate the irradiation period prior to the transient test. About 9% fission gas release occurred from this rod during the irradiation. Test HI-4 consisted of 20 min at a temperature of 2273 ± 50 K in a flowing steam-helium atmosphere. (These temperatures have been revised upward[18] from those referred to in Ref. 16.)

Grain boundary liquefaction of the fuel, i.e., formation of liquid uranium at temperature, was observed in portions of the fuel, principally near large amounts of Zircaloy.[18] As shown in Fig. 1.7, the FASTGRASS-VFP results for fission gas release during test HI-4 under liquefaction conditions are consistent with this observation. The calculations made with the assumption of no fuel liquefaction effects (dashed line) substantially overpredict the reported data. In addition, the FASTGRASS-VFP prediction of <10% increase in grain size is consistent with the observation of no grain growth within a 15% uncertainty range.[17]

### 5. Fission Product Behavior in Trace-irradiated and High-Burnup Fuel During SFD Tests in the PBF Reactor with No Fuel Liquefaction

The SFD-ST experiment[19] consisted of a 32-rod bundle of PWR-type fuel rods, 0.91 m long and enclosed in an insulated shroud. The bundle was subjected to a slow heatup (~2 h) in an oxygen-rich environment to about 1400 K in the lower part of the fuel bundle and about 1800 K in the upper portion of the bundle and then rapid heatup (~10 min) to 2400 K, followed by a rapid quench and coolant reflood. Considerable cladding oxidation and melting, fuel liquefaction, and fuel fragmentation occurred. The SFD 1-1 test[19] also consisted of a 32-rod bundle, but the temperature transient consisted of a rapid heatup (~30 min) in a steam-starved environment to 2400 K followed by a slow cooldown (~20 min) without a rapid quench. The effective burnup levels for SFD-ST and SFD 1-1 are 88.9 and 79.1 MWd/MTU, respectively.

In Fig. 1.8, the measured fission gas release rates for SFD-ST are compared with the release rates predicted by FASTGRASS-VFP on the basis of

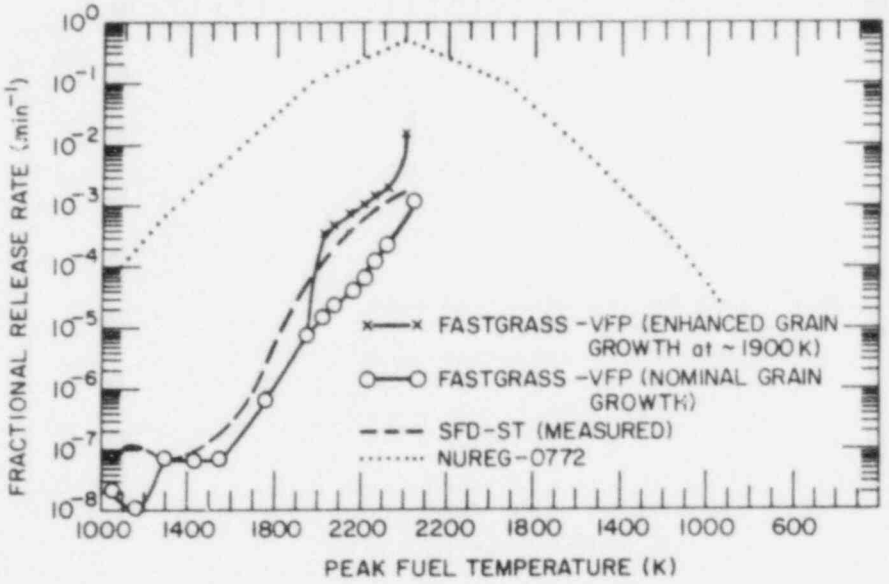


Fig. 1.8. FASTGRASS-VFP Predictions of Fission Gas Release Rates During the SFD-ST Experiment, Compared with the Measured Values and Those Obtained From NUREG-0772.[20]

both the stoichiometric (nominal) and hyperstoichiometric (enhanced) grain growth activation energies. The enhanced grain growth activation energy, which is assumed to be activated at the time when the peak fuel temperatures exceed 1900 K, gives rise to a release rate curve that simulates the trend of the ST data, whereas the nominal value of Q gives release rates that are approximately an order of magnitude below the data at fuel temperatures >1900 K. Such differences in predicted release characteristics due to grain-growth/grain-boundary-sweeping effects are further illustrated in Fig. 1.9, which shows intragranular fission gas retention during SFD-ST as predicted by FASTGRASS-VFP. If nominal grain growth occurs, the majority of the fission gas is predicted to remain trapped within the grain interior, with a total fractional retention of greater than 80% even as fuel temperatures approach 2400 K. However, if the grain growth is enhanced owing to fuel oxidation, a much larger fraction of the intragranular gas is swept to grain boundaries, with only ~10% retention within grains at fuel temperatures of ~2400 K. Such predictions clearly illustrate the important influence of the grain-growth/sweeping process on the morphology and attendant release behavior of gaseous and volatile fission products.

Figure 1.10 shows FASTGRASS-VFP predictions of grain growth in the hottest fuel region of SFD-ST for the cases of nominal and enhanced grain

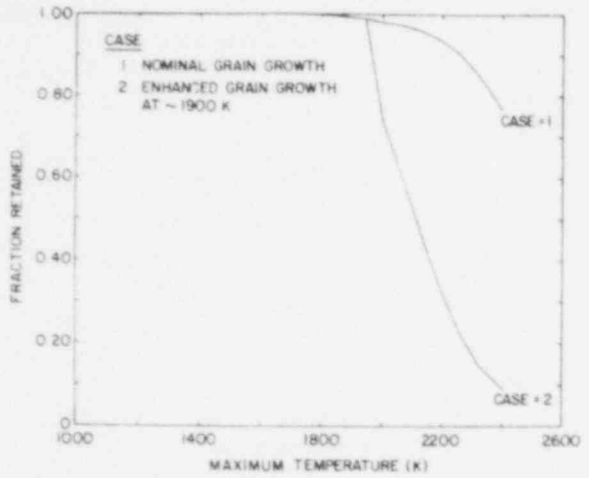


Fig. 1.9

FASTGRASS-VFP Predictions of Fission Gas Retained Intragranularly at the Hottest Fuel Region During the SFD-ST Experiment, Just Prior to Quench.

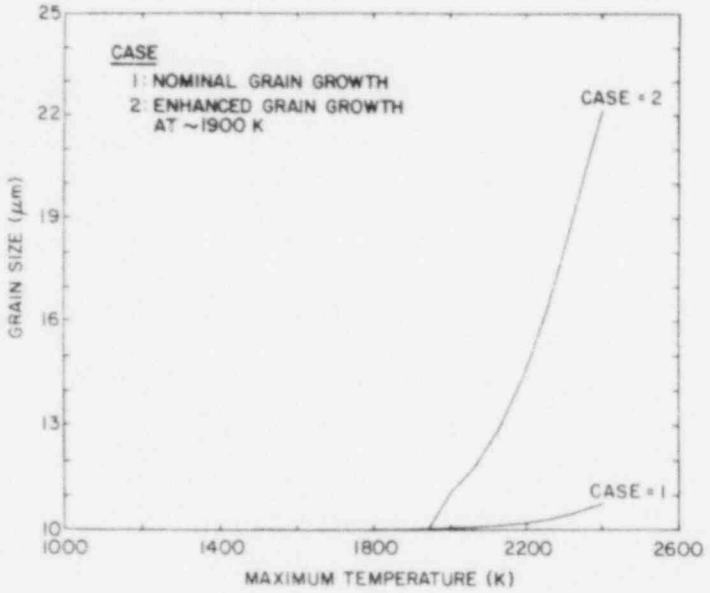


Fig. 1.10

FASTGRASS-VFP Predictions of Grain Growth in the Hottest Fuel Region During the SFD-ST Experiment.

growth. The theory predicts more than a twofold increase in grain size (for a 10-μm initial grain size) when the hyperstoichiometric grain growth activation energy is invoked. Since the steam flow conditions of the SFD-ST scoping test produced an oxidizing environment, enhanced grain growth appears appropriate for this analysis. The analysis is also consistent with the fuel-oxidation-enhanced grain growth noted in the PBF-SFD scoping test,[19] where both $U_4O_9$ precipitates and a substantial increase in grain size were noted upon post-test fuel examination.

In Table 1.1, FASTGRASS-VFP predictions for fission product release during SFD-ST are compared with the measured values. The calculations shown in Table 1.1 were made by assuming that the requench provided the appropriate mechanisms (e.g., fuel fracturing) for the release of the majority of

TABLE 1.1. FASTGRASS-VFP Predictions of Fission Product Release During the SFD-ST Test, Compared with the Measured Values

| Fission Product | Fraction Released | |
|---|---|---|
| | FASTGRASS-VFP Calculation | Collection Tank Measurement |
| Xe | 0.50 | ~0.50[a] |
| Cs | 0.39 | ~0.32 |
| I | 0.51 | ~0.49 |

[a]Obtained from integration of the release rate data.

the fission products predicted to be on the grain boundaries. (FASTGRASS-VFP does not currently contain a model for requench-induced processes, e.g., grain boundary fracturing.)

As was stated previously, the value of the activation energy, Q, for grain boundary motion in hyperstoichiometric $UO_2$ was determined by the requirement that the integrated intragranular Xe release as calculated by FASTGRASS-VFP must be consistent with measured total (end-of-test) release values for SFD-ST. Thus, the agreement between the Xe release predictions and the SFD-ST measured values, shown in Table 1.1, is a consequence of this procedure for determining a value of Q for oxidized $UO_2$. However, the successful interpretation of the HI test series 1-4 (Figs. 1.1, 1.2, 1.4-1.7) and of the trends of the SFD-ST and SFD 1-1 fission gas release rate data (Figs. 1.8 and 1.11), as well as the reasonable agreement between the predicted integral releases of I and Cs and the SFD-ST data (shown in Table 1.1), supports the hypotheses set forth in this paper.

The theory predicts that in the absence of a requench (and fuel liquefaction), very little fission product release would have occurred during SFD-ST. The reason for this result is that owing to the low concentrations of fission gas in this trace-irradiated, low-burnup fuel, very little interconnection of fission gas bubbles is predicted to occur on the grain faces and along the grain edges. This is in contrast to the ORNL

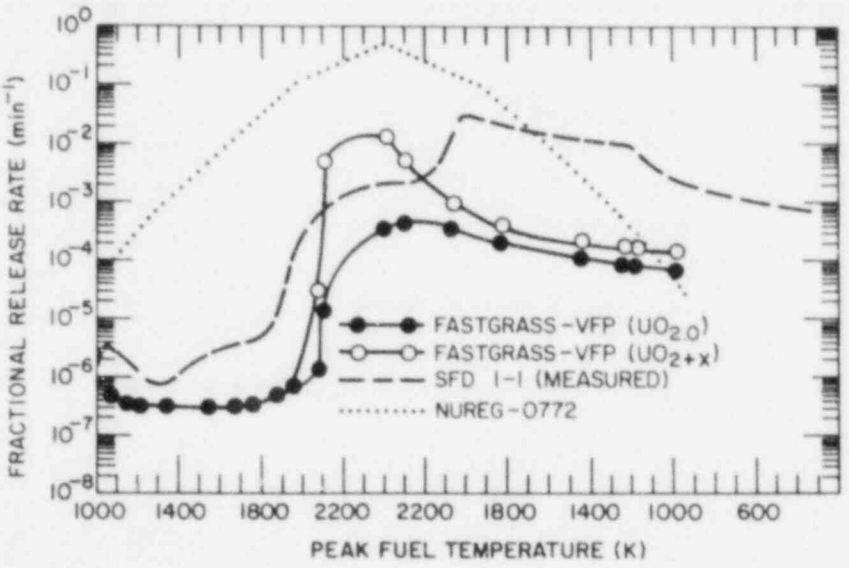


Fig. 1.11. FASTGRASS-VFP Predictions of Fission Gas Release Rates During the SFD 1-1 Experiment, Compared with the Measured Values and Those Obtained From NUREG-0772.

transient tests on high-burnup fuel described earlier. The relatively high concentration of fission gas in the high-burnup fuel enables a high degree of bubble interconnection to occur, with subsequent venting of the retained fission products.

In Figure 1.11, the measured fission gas release rates for the SFD 1-1 test are compared with the release rates predicted by FASTGRASS-VFP for $UO_2$ and $UO_{2+x}$. FASTGRASS-VFP predictions for $UO_{2+x}$ are based on the stoichiometric (nominal) grain growth activation energy for fuel temperatures <1900 K, and on the hyperstoichiometric (enhanced) grain growth activation energy invoked at the time when the peak fuel temperatures exceed 1900 K. The predicted release rates are seen to increase dramatically upon the initiation of grain-growth-induced sweeping of entrapped intragranular bubbles to grain boundaries. Without such grain-growth-induced sweeping, little gas release is predicted for such low-burnup fuel. Such calculations clearly illustrate the point that for low-burnup fuel, in the absence of fuel liquefaction the majority of the fission products remain trapped within the grain interior until elevated temperatures cause sweeping of fission products to grain surfaces and open pores.

Although the initial release characteristics are modeled fairly well by FASTGRASS-VFP, the total fractional release for the SFD 1-1 test is underpredicted by an order of magnitude (i.e., 0.5-2% total predicted release versus ≈20% measured release for the test). This is attributed to the fact that during grain growth, the fission gases are predicted to be swept to grain boundaries, where the gas is trapped. Owing to the absence of quench-induced grain separation in the SFD 1-1 test, and the fact that the gas release that accompanies fuel liquefaction[21] has not been included in the analysis leading to Fig. 1.11, the model predicts gas accumulation at grain surfaces. In actuality the following morphology sequence, leading to fission product release for the SFD 1-1 test, appears probable: (1) initial high gas retention within individual grains due to entrapment of gaseous fission products as individual atoms or intragranular microbubbles, with negligible gas release; (2) grain-growth-induced intragranular microbubble sweeping to grain boundaries at temperatures above ~1900 K, with gas accumulation at grain boundaries and initiation of slow gas release; and (3) destruction of the grain boundary structure by fuel liquefaction (to be discussed in Section 6), with attendant rapid gas release.

Figures 1.8 and 1.11 also show fission gas release rates as a function of fuel temperature for the SFD-ST and SFD 1-1 tests, respectively, as calculated from an extrapolation of the empirical temperature correlations given in NUREG-0772.[20] As indicated earlier, the FASTGRASS-VFP-predicted release rates simulate the trend of the data quite well; however, these rates are about 4 orders of magnitude lower than the predicted rates based upon the NUREG-0772 temperature correlations. This discrepancy is due, in part, to the fission product morphology characteristics of the trace-irradiated fuel employed in the SFD-ST and SFD 1-1 tests. The NUREG-0772 correlations were developed primarily from release experience for medium- to high-burnup fuel under relatively isothermal test conditions; in contrast, the SFD-ST and SFD 1-1 tests were non-isothermal, and the fuel used in these tests was essentially fresh (except for the development of a small inventory of fission products at an effective burnup level of approximately 0.0089 at.%). FASTGRASS-VFP analyses indicate that for trace-irradiated fuel, the vast majority of both fission gases and volatiles (I and Cs) are still retained within the interior of individual grains either

as individual atoms or as newly nucleated intragranular microbubbles. FASTGRASS-VFP calculations indicate that such morphology will exist until grain growth causes the sweeping of intragranular microbubbles to grain boundaries. Since grain growth normally requires fuel temperatures in excess of 1900 K, significant release during the heatup phase of these PBF/SFD tests is precluded. Only when temperatures above 1900 K cause destruction of the grain boundary structure (by liquefaction, eutectic fuel melting and/or quench-induced processes such as grain boundary fracturing) is significant release predicted for such low-burnup fuel.

The effect of burnup on fission product release and grain growth is further demonstrated in Figs. 1.12-1.15, which show FASTGRASS-VFP predictions for SFD 1-1 accident conditions as a function of as-irradiated burnup. These calculations do not include the effects of fuel liquefaction and quench-induced release processes (see Section 6). Figs. 1.12-1.13 and 1.14-1.15 show results for $UO_2$ and $UO_2/UO_{2+x}$ fuel compositions, respectively (i.e., analogous to the two FASTGRASS-VFP curves shown in Fig. 1.10). Figure 1.12 shows that for $UO_2$, the fractional transient gas release increases with irradiation time to a maximum value of 13.8% at 6 at.% burnup. The reason for this increase in transient gas release with as-irradiated burnup is that the higher-burnup fuel develops more and larger fission gas bubbles on the grain boundaries, which provide an increased degree of interconnection to a free surface. The transient gas release from $UO_2$ is limited to relatively moderate values because of the limited degree of grain growth, as shown in Fig. 1.13. Transient fission gas release for $UO_2/UO_{2+x}$ fuel compositions is predicted to increase dramatically as the as-irradiated burnup is increased from 0.01 to ~3 at.% (see Fig. 1.14). However, above ~3 at.% burnup, the predicted fission gas release decreases and tends to saturate at a relatively constant value. Again, the reason for the dramatic increase in transient gas release for burnups between 0.01 and 3 at.% is the increased degree of interconnection of grain boundary porosity to a free surface. At burnups > 3 at.%, however, the fission gas release is limited by a substantial decrease in the grain boundary sweeping of intragranular gas to the grain surface; this is due to a decrease in the predicted grain growth, which is a consequence of the increased development of fission gas bubbles on the grain boundaries (see Fig. 1.15).

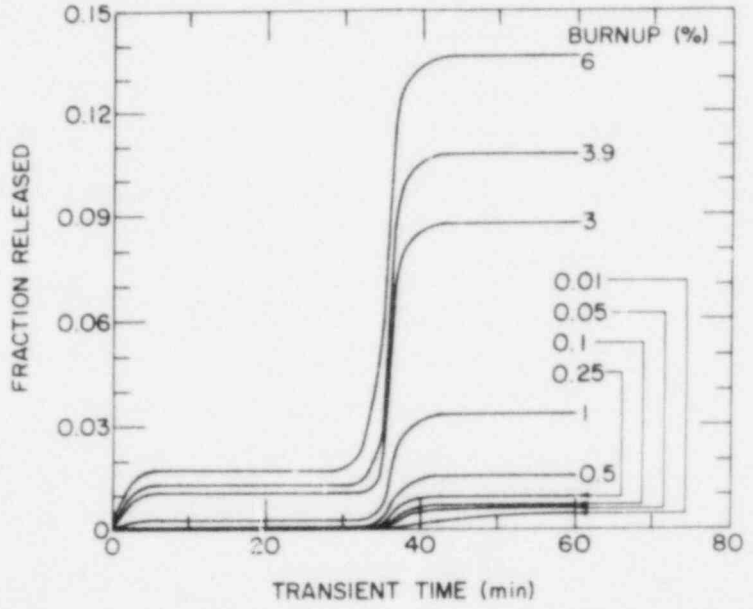


Fig. 1.12. FASTGRASS-VFP Predictions of Fission Gas Release During the SFD 1-1 Experiment For $UO_2$ Fuel Composition, as a Function of Fuel Burnup.

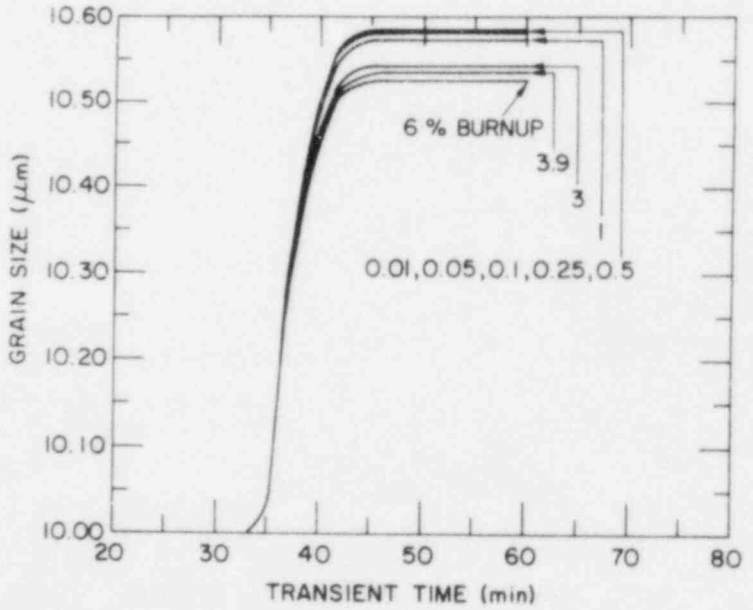


Fig. 1.13. FASTGRASS-VFP Predictions of Grain Growth During the SFD 1-1 Experiment For $UO_2$ Fuel Composition, as a Function of Fuel Burnup.

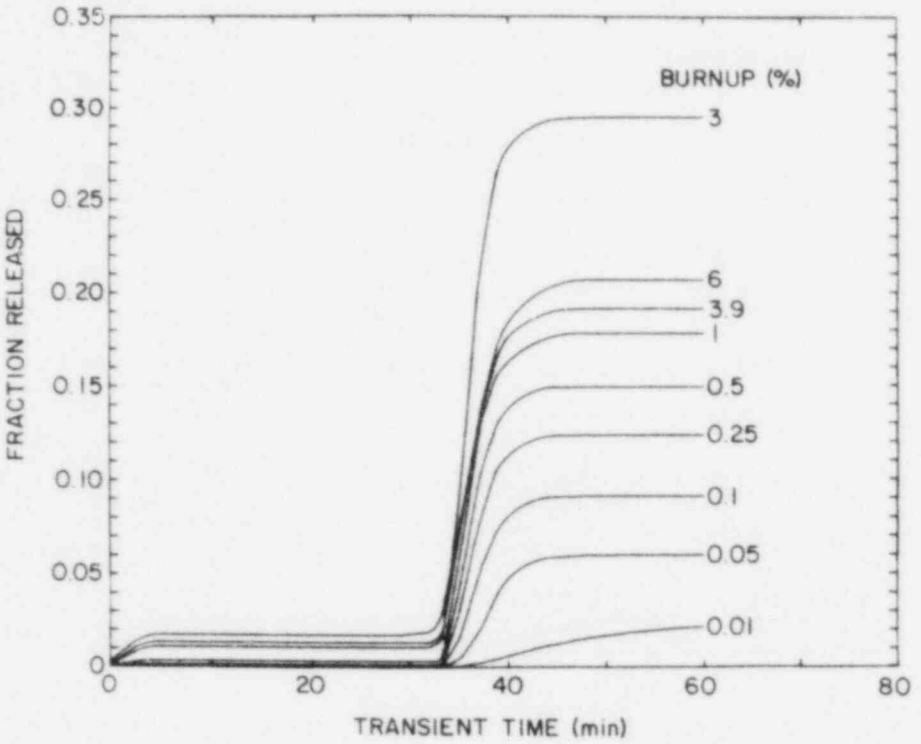


Fig. 1.14. FASTGRASS-VFP Predictions of Fission Gas Release During the SFD 1-1 Experiment For $UO_2/UO_{2+x}$ Fuel Compositions, as a Function of Fuel Burnup.

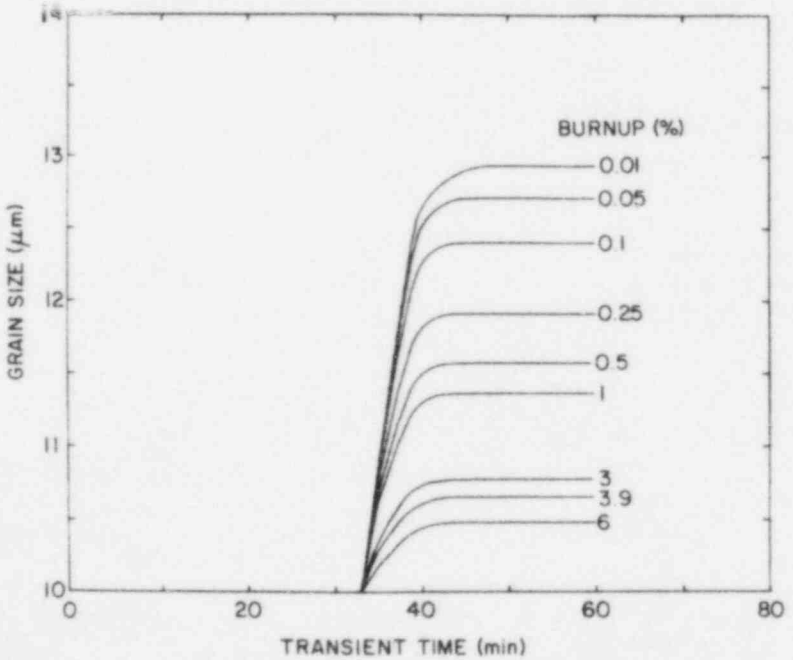


Fig. 1.15. FASTGRASS-VFP Predictions of Grain Growth During the SFD 1-1 Experiment for $UO_2/UO_{2+x}$ Fuel Compositions, as a Function of Fuel Burnup.

## 6. Fission Product Behavior in Trace-irradiated and High-Burnup Fuel During SFD Tests in the PBF Reactor with Fuel Liquefaction

Figure 1.16 shows the results of FASTGRASS-VFP calculations for SFD 1-1 type accident conditions with and without the effects of fuel liquefaction. As discussed in Section 5, the predicted release in the absence of fuel liquefaction and/or dissolution is much lower than the measured amounts. The theory predicts an enhanced release of fission gas from this trace-irradiated fuel subsequent to fuel liquefaction (solid curve in Fig. 1.16). FASTGRASS-VFP analyses of the SFD 1-1 test indicate that significant liquefaction release during the test depends on the initial coalescence and growth of relatively small (~0.04-μm-diameter) bubbles in the liquefied material due to a volume diffusion mechanism. Whereas volume diffusion (i.e., self diffusion of the $U^{4+}$ ion) is relatively slow in solid $UO_2$, it appears to be a significant factor in the motion of small bubbles in liquefied $UO_2$. The growth of small bubbles in the liquefied material is predicted to occur mainly by the volume diffusion mechanism until the bubbles reach sufficient size such that their mobility by viscous flow is high enough to promote appreciable bubble sweep-up. Subsequently, the release of fission gas (and other fission products trapped in the bubbles) is dominated

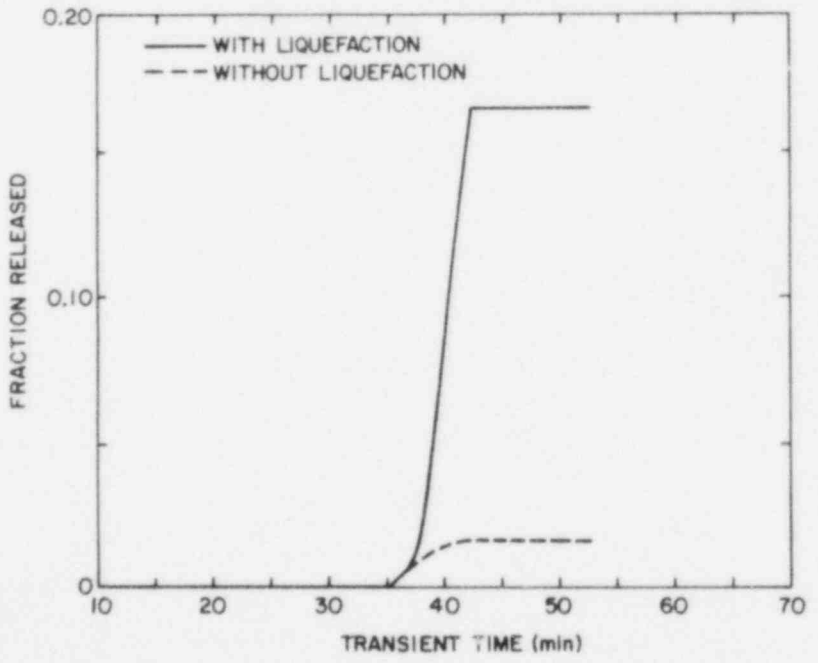


Fig. 1.16. FASTGRASS-VFP Predictions of Fission Gas Release During the SFD 1-1 Experiment With and Without the Effects of Fuel Liquefaction.

by the motion of relatively large bubbles (~1 μm diameter) under buoyant forces. The FASTGRASS-VFP result for total fission gas release during SFD 1-1 with liquefaction (solid curve in Fig. 1.16) is in reasonable agreement with the measured quantity.[19] In trace-irradiated fuel, because of the low level of interconnected porosity, fuel liquefaction provides the major release paths.

In high-burnup fuel, under fuel liquefaction conditions, the resultant enhanced growth of fission gas bubbles in the liquefied material surrounding the grains reduces grain growth rates and grain boundary sweeping of intragranular fission products into the liquefied lamina. In addition, just subsequent to fuel liquefaction in high-burnup fuel, fission product release rates are reduced owing to a decreased mobility in a viscous medium as compared to vapor transport through interconnected tunnels. This situation is evident in Fig. 1.17, which shows the predictions of the theory for a SFD 1-1 type accident scenario with fuel irradiated to 3 at.% burnup. As shown in Fig. 1.17, the occurrence of fuel liquefaction reduces the fission gas release rates and the overall fission gas released is less than that predicted to be released with no fuel liquefaction.

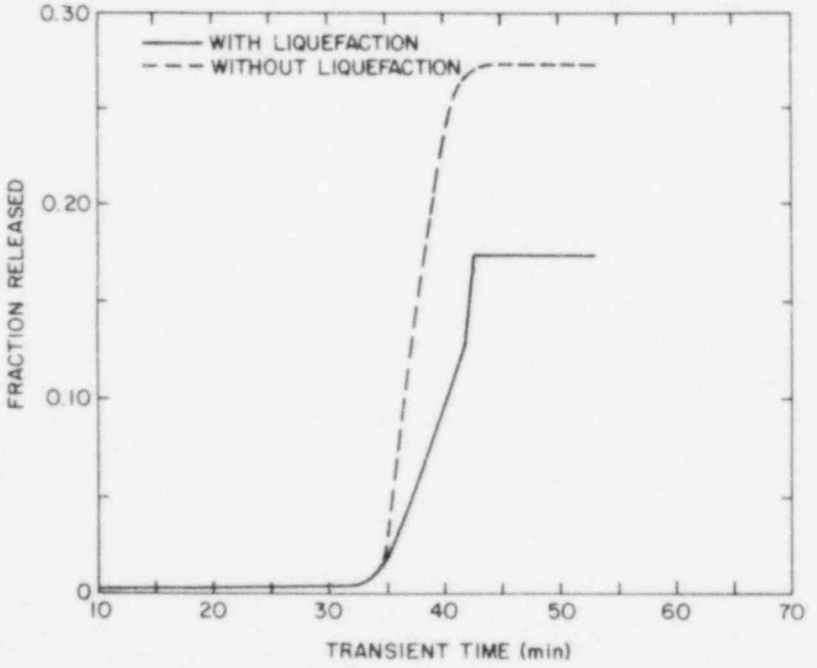


Fig. 1.17. FASTGRASS-VFP Predictions of Fission Gas Release From Fuel Irradiated to 3 at.% Burnup and Subjected to a SFD 1-1 Test Scenario With and Without the Effects of Fuel Liquefaction.

Fuel temperatures in SFD 1-1 exceeded the U-Zr eutectic melting temperature (these revised temperatures have not been used in the analysis presented here), and gross $UO_2$ dissolution was observed in addition to $UO_2$ liquefaction.[22] FASTGRASS-VFP results for the case of gross $UO_2$ dissolution indicate an enhanced release for both trace-irradiated and high-burnup fuel under SFD 1-1 type accident scenarios. A description of the FASTGRASS-VFP dissolution theory and results for SFD accident conditions will be presented in future publications.

## 7. Conclusions

The results of the FASTGRASS-VFP analysis indicate that for the SFD-ST and SFD 1-1 tests, the sequence of events leading to fission product release appears to be as follows: (1) initial high fission-product retention within individual grains due to entrapment of fission products as individual atoms or intragranular microbubbles, with negligible release; (2) grain-growth-induced intragranular atomic and microbubble sweeping to grain boundaries at temperatures in excess of 1900 K, with attendant bubble growth and gas accumulation at the grain boundaries and initiation of slow gas and VFP release; and (3) destruction of the grain boundary structure via fuel liquefaction and/or quench-induced processes (e.g., grain boundary fracturing), with attendant rapid intergranular gas release. Subsequently, enhanced release due to gross dissolution (eutectic melting) may occur.

FASTGRASS-VFP theory is in reasonable agreement with the observed fission product behavior of high-burnup fuel during the ORNL high-temperature heating tests. The results of the analysis indicate that a grain-growth/grain-boundary-sweeping mechanism is responsible for the relatively large intragranular fission product release predicted to occur during the majority of these tests. FASTGRASS-VFP-predicted grain sizes for tests HI-1, HI-2, HI-3 and HI-4 are in reasonable agreement with grain growth observations made on the tested fuel. The measured grain growth for the high-burnup fuel used in these ORNL high-temperature heating tests is substantially less than the observed grain growth for the PBF tests on trace-irradiated fuel. These results are interpreted in the context of the theory for grain-growth/grain-boundary-sweeping in that the accumulation of

fission products on the grain boundaries of high-burnup fuel retards grain boundary movement.

The FASTGRASS-VFP model for the behavior of fission products during fuel liquefaction conditions was applied to the interpretation of the NRC-sponsored SFD tests in the PBF reactor, and the HI test series performed at ORNL. Initial results indicate that whereas fuel liquefaction leads to an enhanced release of fission products in trace-irradiated fuel, the occurrence of fuel liquefaction in high-burnup fuel can degrade fission product release. In trace-irradiated fuel, because of the low level of interconnected porosity, fuel liquefaction provides the major release paths. In high-burnup fuel, under fuel liquefaction conditions, the resultant enhanced growth of fission gas bubbles in the liquefied material reduces grain growth rates and grain boundary sweeping of intragranular fission products into the liquefied region. In addition, just subsequent to fuel liquefaction in high-burnup fuel, fission product release rates are reduced because of the decreased mobility of gas bubbles in a viscous medium as compared to vapor transport through interconnected tunnels. FASTGRASS-VFP fission gas release and grain growth results for ORNL tests HI-3 (minimal liquefaction observed, fuel temperature = 2273 K) and HI-4 (fuel liquefaction observed in the form of a U-rich melt phase on the grain boundaries, temperature = 2273 K) are in good agreement with the reported results. Test HI-3 had about 60% fission gas release, while HI-4 had about 20% release. Grain size in HI-3 increased by about 50%, while HI-4 had no grain growth within the 15% experimental uncertainties. The analyses also indicate that gross $UO_2$ dissolution due to U-Zr eutectic melting leads to enhanced release for both trace-irradiated and high-burnup fuel.

The results of FASTGRASS-VFP analyses indicate a need for caution when extrapolating the NUREG-0772 correlations, which are based primarily upon medium- to high-burnup data, to determine release characteristics for the trace-irradiated fuel employed in the PBF tests. This is because at extremely low burnup, there does not exist a sufficient inventory of fission gases to precipitate the development of a network of interconnected porosity necessary for gas release from the fuel interior to the pellet surface. Only upon initiation of enhanced grain growth at elevated temperatures

(>1900 K), and destruction of the grain boundary structure by liquefaction and/or quench-induced processes, would significant release be expected for these low-burnup conditions.

## B. References for Chapter I


1. J. Rest, "Volatile Fission-Product Source Term Evaluation Using the FASTGRASS Computer Code," pp. 111-121 in Proceedings of the International Meeting on Thermal Nuclear Reactor Safety, Chicago, Ill., August 29-September 2, 1982, NUREG/CP-0027, Vol. 1 (February 1983).

2. J. Rest, Evaluation of Volatile and Gaseous Fission Product Behavior in Water Reactor Fuel Under Normal and Severe Core Accident Conditions, Nucl. Technol. **61**, 33-48 (1983).

3. J. Rest, An Improved Model For Fission Product Behavior in Nuclear Fuel Under Normal and Accident Conditions, J. Nucl. Mater. **120**, 195-212 (1984).

4. J. Rest, "The Mechanistic Prediction of Fission Gas, Iodine, and Cesium Release from LWR Fuel Under Degraded-Core Accident Conditions," in Proceedings of the Topical Meeting on Fission Product Behavior and Source Term Research, Snowbird, Utah, July 15-19, 1984 (in press).

5. J. Rest, The Coupled Kinetics of Grain Growth and Fission Product Behavior in Nuclear Fuel Under Degraded-Core Accident Conditions, J. Nucl. Mater. (in press).

6. M. V. Speight and G. W. Greenwood, Grain Boundary Mobility and Its Effect in Materials Containing Inert Gases, Philos. Mag. 9, 683 (1964).

7. D. R. Olander, p. 320 in Fundamental Aspects of Nuclear Reactor Fuel Elements, U. S. Technical Information Center, USERDA (1976).

8. J. Belle, pp. 512-515 in Uranium Dioxide, U. S. Government Printing Office, Washington, DC (1961).

9. J. T. Bittel, L. H. Sjodahl, and J. F. White, Steam Oxidation Kinetics and Oxygen Diffusion in $UO_2$ at High Temperatures, J. Am. Ceram. Soc. **52**, 445 (1969).

10. J. R. MacEwan and J. Hayashi, pp. 245-272 in Nuclear and Engineering Ceramics, British Ceramic Society, Stoke-on-Trent, U.K. (1967).

11. J. A. Turnbull, "A Review of Rare Gas Diffusion in Uranium Dioxide" (unpublished work, 1972).

12. P. Hofmann and D. Kerwin-Peck, in Proceedings of the International Meeting on Light Water Reactor Severe Accident Evaluation, Cambridge, Mass., August 28-September 1, 1983, Vol. I, American Nuclear Society, LaGrange Park, Ill. (1983).

13. W. Dienst, P. Hofmann, and D. Kerwin-Peck, Chemical Interactions Between $UO_2$ and Zircaloy-4 From 1000-2000°C, Nucl. Technol. 65, 109-124 (1984).

14. S. Brets Znajdar, Prediction of Transport and Other Physical Properties of Fluids. Pergamon Press, Oxford (1971).

15. R. M. Cornell, The Growth of Fission Gas Bubbles in Irradiated Uranium Dioxide, Philos. Mag. 19, 539 (1969).

16. M. F. Osborne et al., in Proceedings of the Topical Meeting on Fission Product Behavior and Source Term Research, Snowbird, Utah, July 15-19, 1984 (in press).

17. R. V. Strain, ibid.

18. R. V. Strain, private communication.

19. D. J. Osetek, R. R. Hobbins, K. Vinjamuri, and A. W. Cronenberg, in Proceedings of the Topical Meeting on Fission Product Behavior and Source Term Research, Snowbird, Utah, July 15-19, 1984 (in press).

20. U. S. Nuclear Regulatory Commission, Technical Basis for Estimating Fission Product Behavior During LWR Accidents, NUREG-0772 (June 1981).

21. A. W. Cronenberg et al., "An Assessment of Liquefaction-induced I, Cs, and Te Release from Low and High Burnup Fuel," pp. 4.5-1 to 4.5-8 in Proceedings of the International Meeting on Light Water Reactor Severe Accident Evaluation, Cambridge, Mass., August 28-September 1, 1983, Vol. I, American Nuclear Society, LaGrange Park, Ill. (1983).

22. B. Cook, private communication.

# II. CLAD PROPERTIES FOR CODE VERIFICATION

Principal Investigator:
H. M. Chung

The Zircaloy cladding of fuel rods in light-water-cooled reactors is susceptible to local breach-type failures, commonly known as pellet-cladding interaction (PCI) failures, during power transients after the fuel has achieved sufficiently high burnup. As a result of the high burnup, the gap between the $UO_2$ fuel pellets and the cladding is closed and highly localized stress is believed to be imposed on the cladding during power transients by differential thermal expansion of the cracked fuel and cladding. In addition to the localized stress, a high-burnup fuel cladding is also characterized by high-density radiation-induced defects, mechanical constraints imposed by pellet-cladding friction, compositional changes (e.g., oxygen and hydrogen uptake associated with in-service corrosion), and geometrical changes due to creep-down and bowing. It is possible that synergistic effects involving more than one of the above factors influence the deformation and fracture of the in-reactor fuel cladding, e.g., strain aging associated with impurity or alloying elements, irradiation- or stress-induced segregation of the elements, and subsequent formation of nonequilibrium phases. Although mechanisms of stress corrosion cracking associated with volatile fission products such as I and liquid metal embrittlement associated with elements such as Cd have been well established for local breach-type failures of irradiated and unirradiated Zircaloy cladding under out-of-reactor simulation conditions, conclusive evidence of these processes is not yet available for in-reactor PCI failures. Consequently, to provide a better understanding of the PCI phenomenon, we have undertaken a mechanistic study of the deformation and fracture behavior of actual power-reactor fuel cladding discharged after a high burnup.

In this program, the effect of temperature, strain rate, and stress localization on the deformation and fracture characteristics of Zircaloy cladding from spent-fuel rods is being investigated by means of internal gas-pressurization and mandrel-loading experiments in the absence of simulated fission product species. The deformed and fractured specimens of spent-fuel cladding are examined by optical microscopy, scanning electron microscopy

(SEM), transmission electron microscopy (TEM), and high-voltage electron microscopy (HVEM). The results of microstructural and fracture-property investigations will be used to develop a failure criterion for the cladding under PCI-type loading conditions. The information will be incorporated into fuel performance codes, which can be used to evaluate the susceptibility of extended-burnup fuel elements in commercial reactors to PCI failures during power transients in later cycles, and to evaluate cladding performance and reliability of new fuel-element designs. An optimization of power ramp procedures to minimize cladding failures would result in a significant decrease in radiation exposure of plant personnel due to background and airborne radioactivity as well as an extension of core life in terms of allowable off-gas radioactivity.

## A. TEM-HVEM Characterization of Bulk Precipitates of Cubic $ZrO_2$ and Hydride in Brittle-Failure Zircaloy Tubes

### 1. Introduction

TEM-HVEM analysis of the microstructure of the H. B. Robinson Zircaloy-4 cladding tube 217A4G, which failed in a brittle manner during the modified expanding-mandrel test at 325°C, has been reported previously.[1] By means of "$2\frac{1}{2}$D microscopy," stereopairs of weak-beam dark-field images were obtained that show copious bulk precipitates of cubic $ZrO_2$ and hydrides in thin-foil specimens from regions adjacent to the brittle fracture site. The brittle fracture was associated with those bulk precipitates. In this reporting period, similar characteristic microstructures were also observed in Big Rock Point Zircaloy-2 cladding tubes 165AG10 and 165AE4B, which failed in a brittle manner during internal gas-pressurization tests at 325°C.[2] It was further determined that the bulk hydride (35-100 nm in size) was the $\delta$ rather than the $\gamma$ hydride of zirconium.

### 2. Big Rock Point Reactor Zircaloy-2 Cladding Tubes

The brittle-failure specimens 165AG10 and 165AE4B showed "pseudocleavage-plus-fluting" features on the fracture surface extending up to ~95 and ~78% of the wall thickness, respectively.[2] Disk specimens 6.3 mm in

diameter, which contain the pinhole failure site at the center, were ultrasonically cored from the tubes. The disks were split open at room temperature to reveal the fracture surfaces. TEM specimens (3-mm diam) were obtained from the split disks after SEM fractographic examination.

HVEM microstructures obtained from a 3-mm-diam foil specimen of the 165AE4B tube are shown in Fig. 2.1. The indexed selected-area diffraction (SAD) pattern of Fig. 2.1(B) shows the $(1\bar{2}3)$ zone of the cubic $ZrO_2$ and the $(\bar{1}11)$ and $(1\bar{1}\bar{1})$ reflections of the δ hydride. The d-spacing of the δ-hydride reflections is 0.276 nm. The $(\bar{1}11)$ and $(1\bar{1}\bar{1})$ reflections of the γ hydride (d-spacing 0.272 nm) are not compatible with the SAD pattern. Stereopairs of weak-beam dark-field images of the $(\bar{1}11)$ and $(1\bar{1}\bar{1})$ reflections of the cubic $ZrO_2$, δ hydride, and surface χ hydride are shown, respectively, in Figs. 2.1(C) and (D). The bulk nature of the cubic-$ZrO_2$ and δ-hydride precipitates, similar to that reported for the H. B. Robinson Reactor Zircaloy-4 cladding tube 217A4G,[1] is evident from the figures. Figure 2.1(E) shows a stereopair of the dark-field images obtained from the double diffraction spots of the $(1\bar{1}\bar{1})$ reflections of the same three phases as Fig. 2.1(D). The SAD pattern obtained from another region of the 165AE4B thin-foil specimen and indexed in Fig. 2.2(B) shows (310) zones of the cubic $ZrO_2$ and the δ hydride. The d-spacing of the (002) reflections of the δ hydride, i.e., 0.239 nm, is compatible with the pattern, but the 0.247-nm d-spacing of the (002) reflections of the γ hydride is not. A stereopair of the (002) reflections of the cubic-$ZrO_2$ and δ-hydride precipitates is shown in Fig. 2.2(C). The integrated intensities of the precipitate reflections in the SAD patterns of Figs. 2.1(B) and 2.2(B) indicate that the volume fraction of the cubic $ZrO_2$ is at least several times larger than that of the δ hydride. This is consistent with the dark-field images shown in the figures. The sharpness of the δ-hydride reflections compared to the diffuse spots of the cubic $ZrO_2$ is also consistent with the size and morphologies of the precipitates.

Similar microstructures containing copious precipitates of the bulk cubic $ZrO_2$ and δ hydride were observed in the 165AG10 tube. Some typical examples are shown in Figs. 2.3 and 2.4. In contrast to the observations for the 165AE4B tube, the volume fraction of the δ hydride in Figs. 2.3 and 2.4 appears to be similar to that of the cubic $ZrO_2$. The SAD pattern of

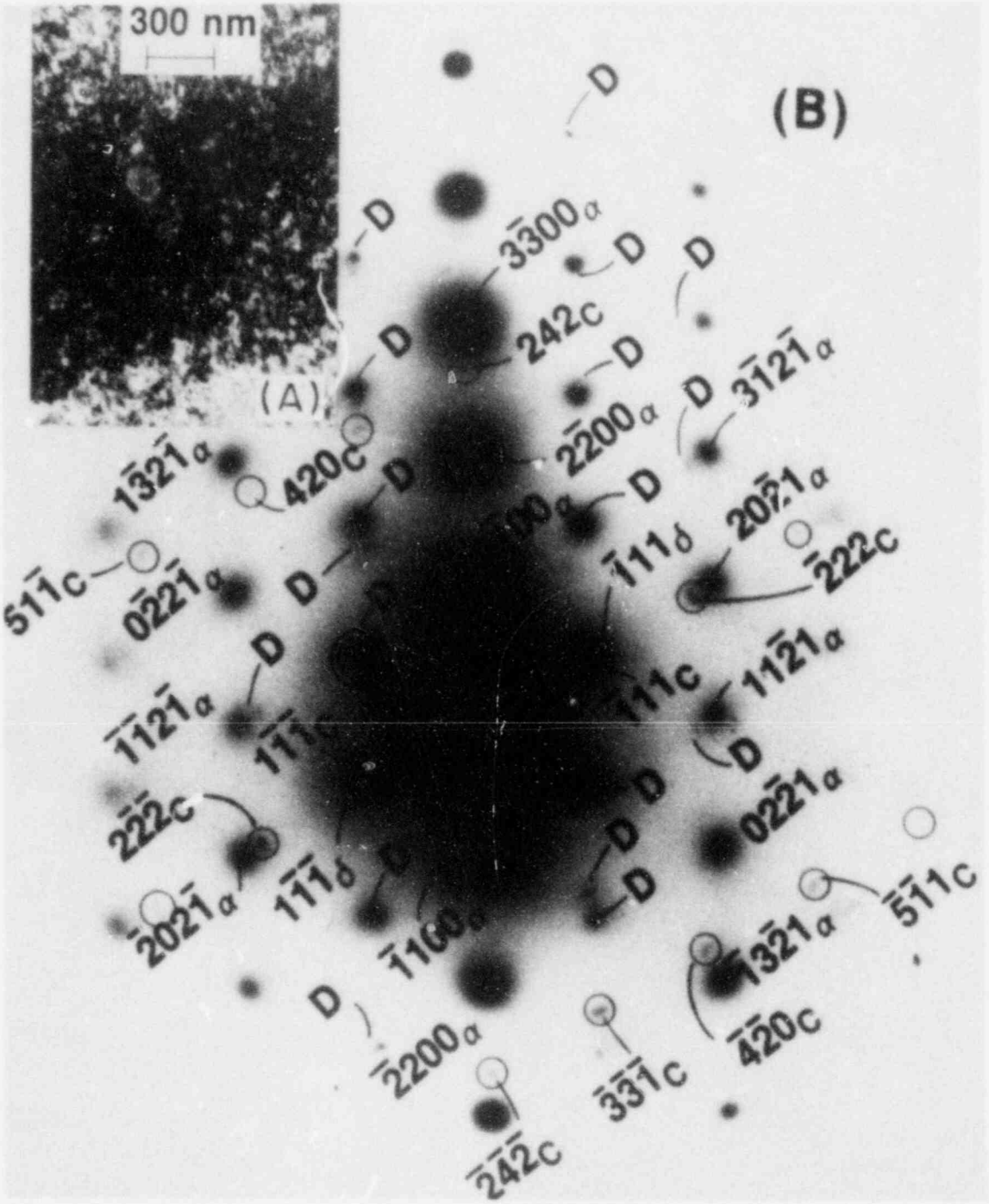


Fig. 2.1. HVEM Micrographs Obtained from Brittle-Fracture Site of Big Rock Point Cladding Tube 165AE4B after Internal Gas-Pressurization Test at 325°C. (A) Bright-field image of recrystallized grain; (B) indexed SAD pattern showing $(1\bar{2}3)$ zone of the cubic $ZrO_2$ and $(\bar{1}11)$ and $(1\bar{1}\bar{1})$ reflections of the δ hydride; (C) dark-field stereopair obtained from the $(\bar{1}11)$ reflections of the cubic $ZrO_2$, δ hydride, and surface hydride; (D) similar stereopair from the $(1\bar{1}\bar{1})$ reflection; (E) stereopair from the double diffraction spot of the $(1\bar{1}\bar{1})$ reflection denoted by the circles in (B).

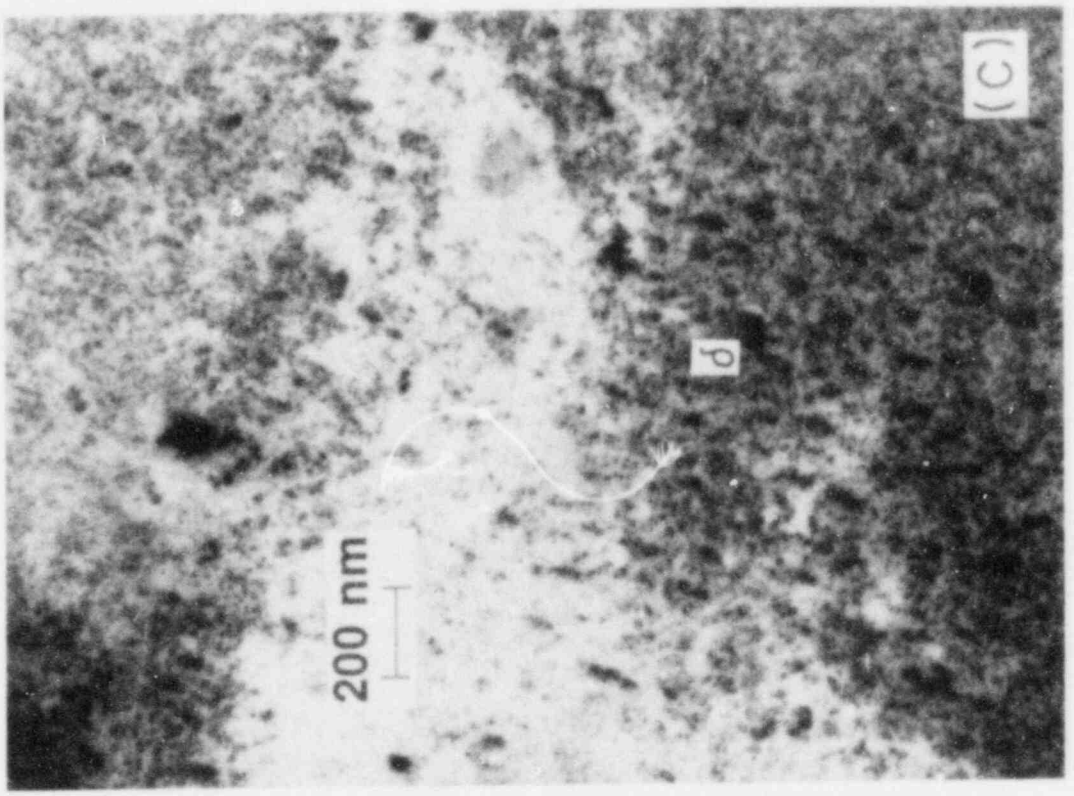


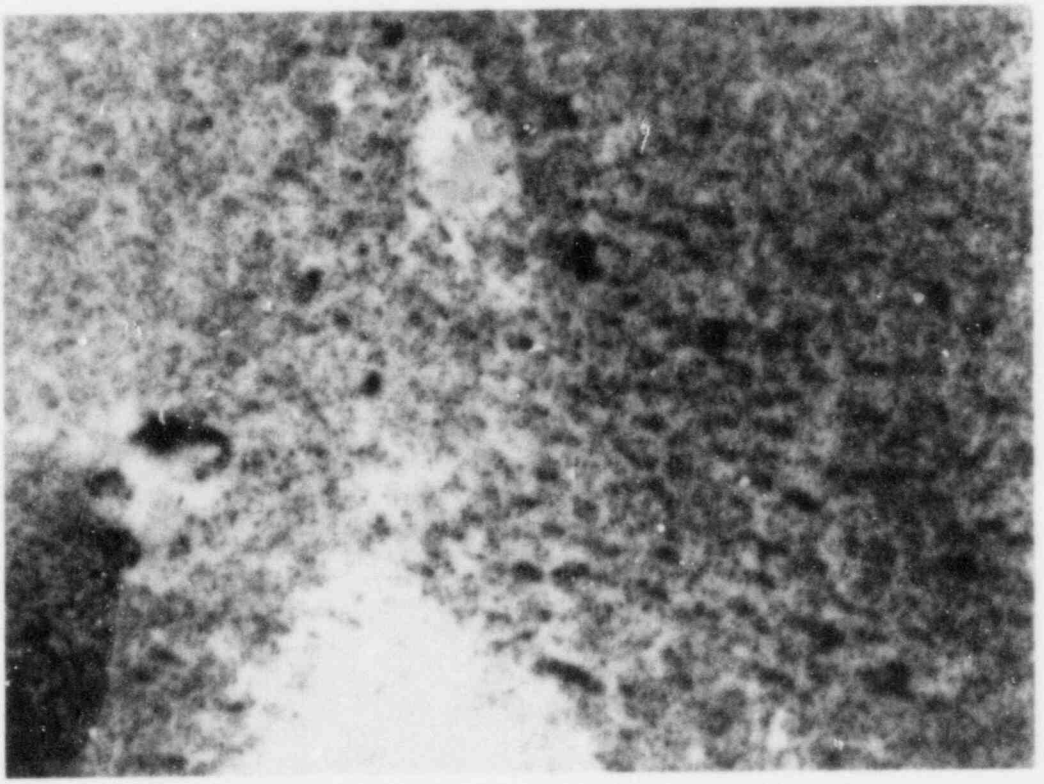

Fig. 2.1. (Contd.)

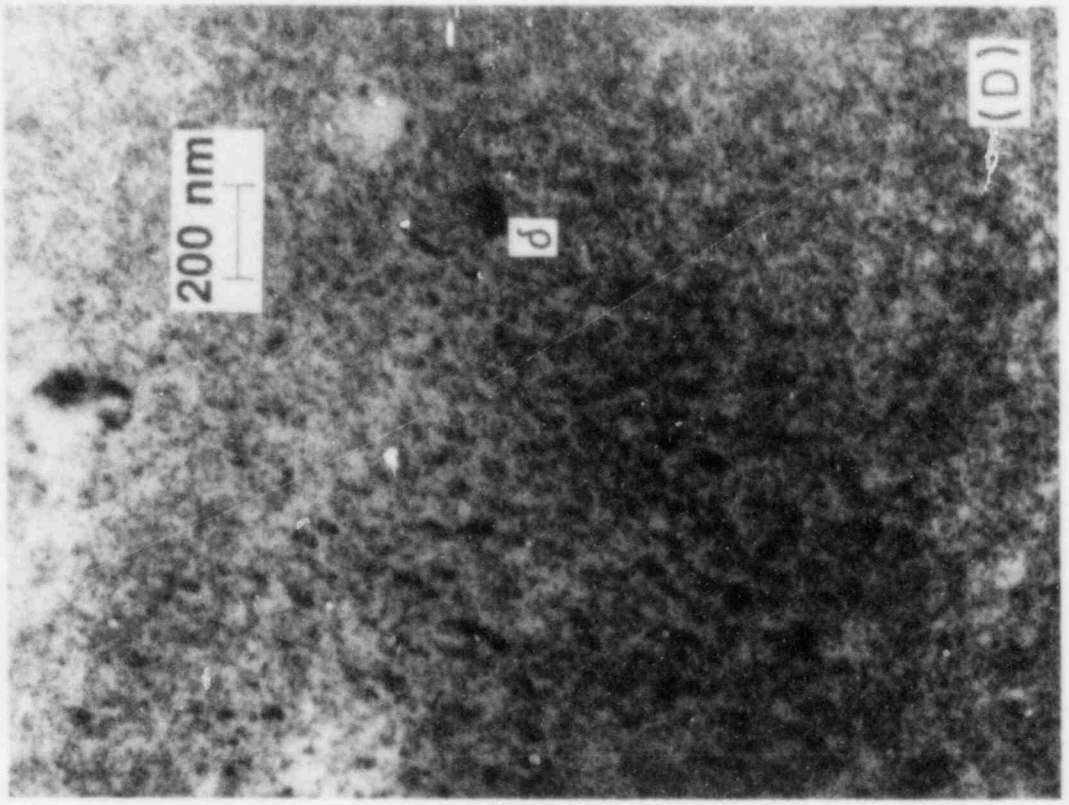


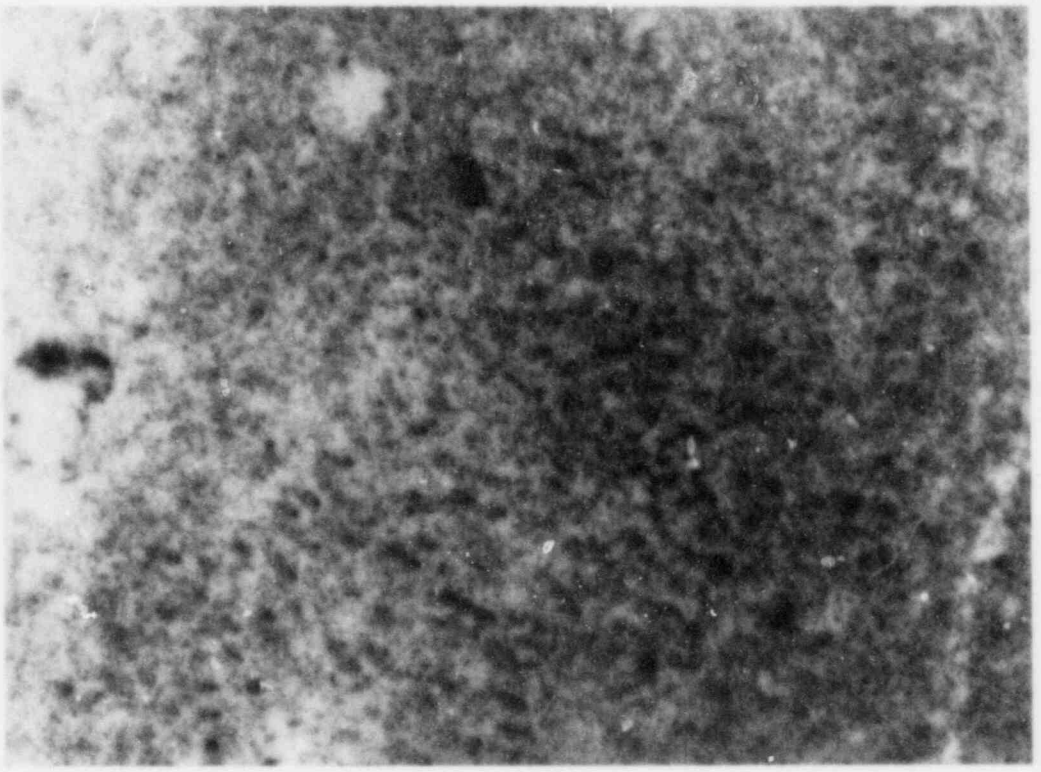

Fig. 2.1. (Contd.)

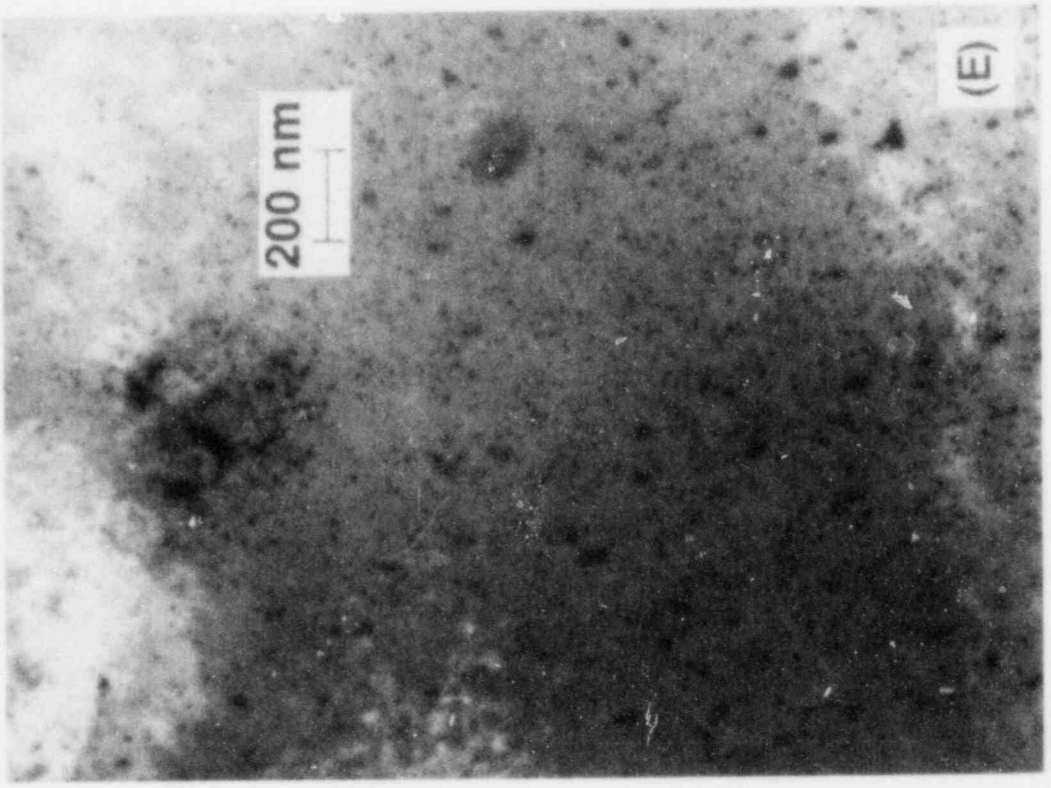


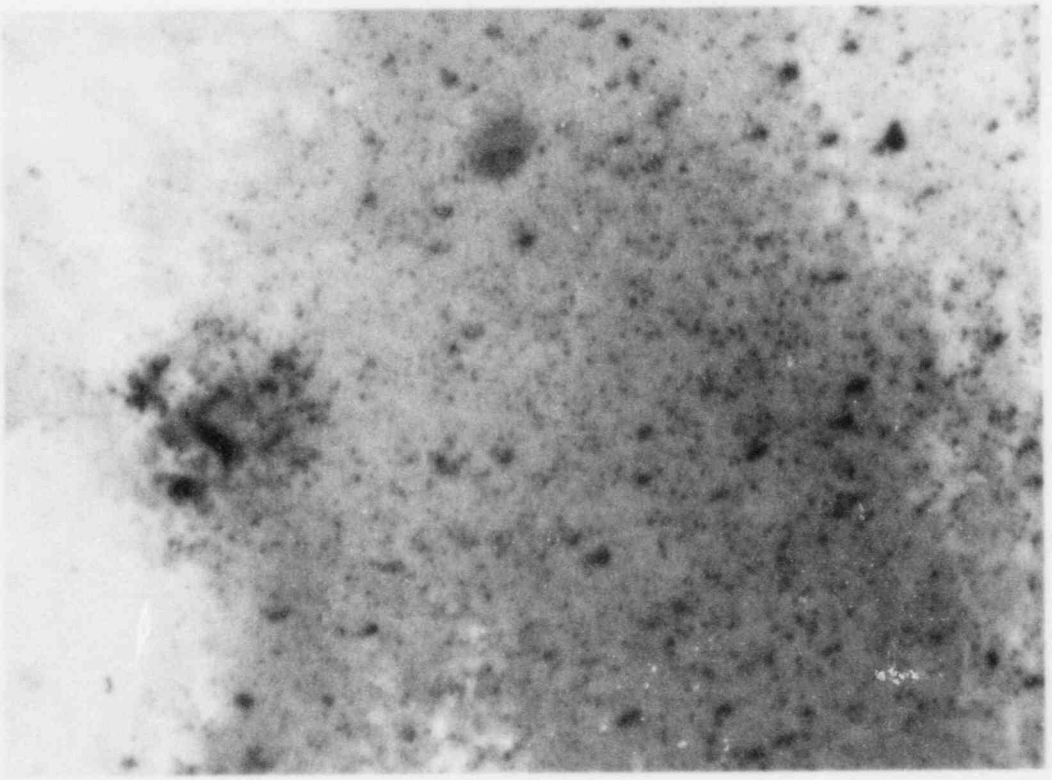

Fig. 2.1. (Contd.)

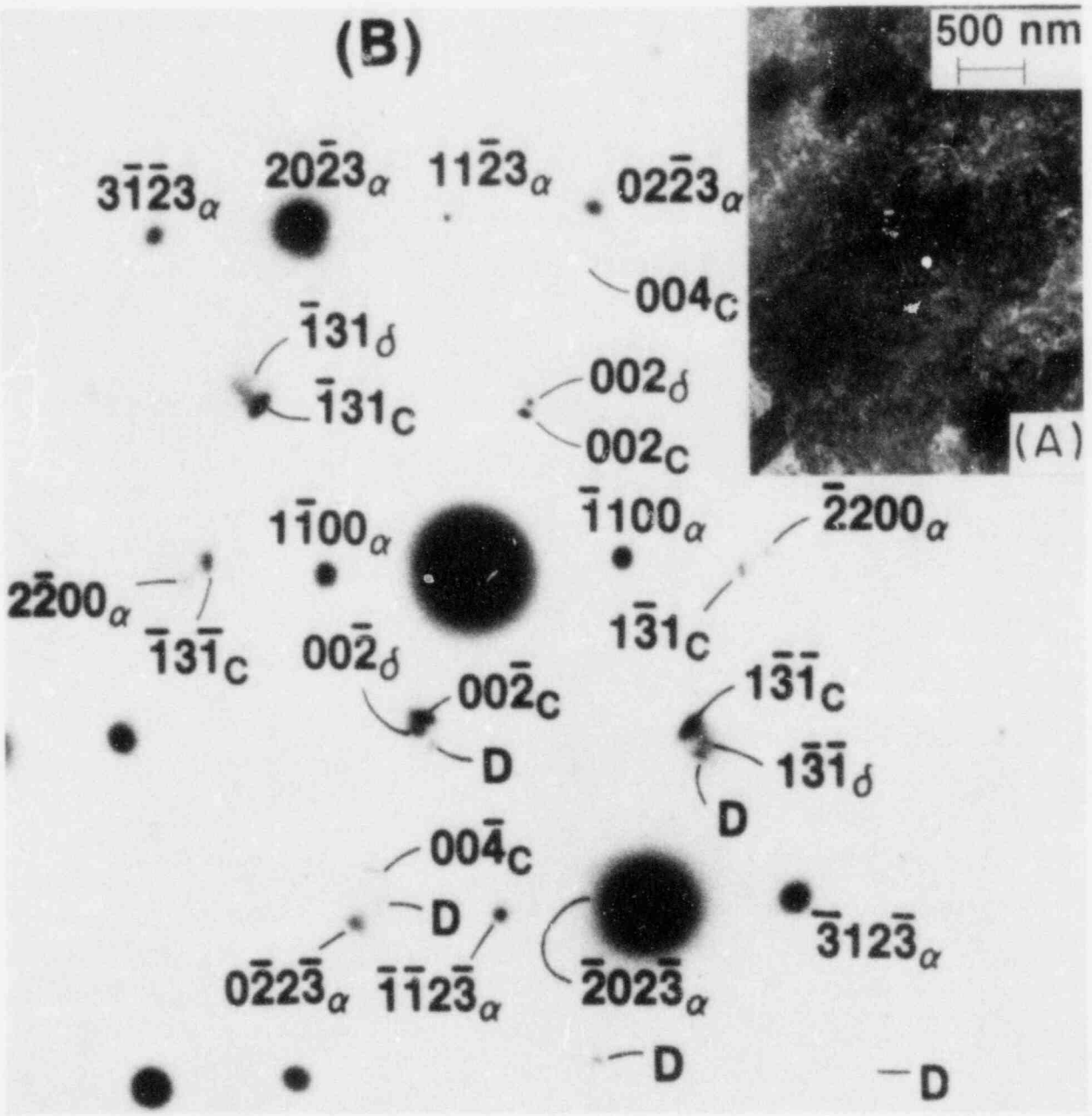


Fig. 2.2. HVEM Micrographs from a Different Region of Cladding Tube 165AE4B. (A) Bright-field image; (B) indexed SAD pattern showing (310) zones of the cubic $ZrO_2$ and δ hydride; (C) dark-field stereopair obtained from the (002) reflections of the cubic $ZrO_2$ and δ hydride. The letter δ denotes the bulk δ hydrides in (C).

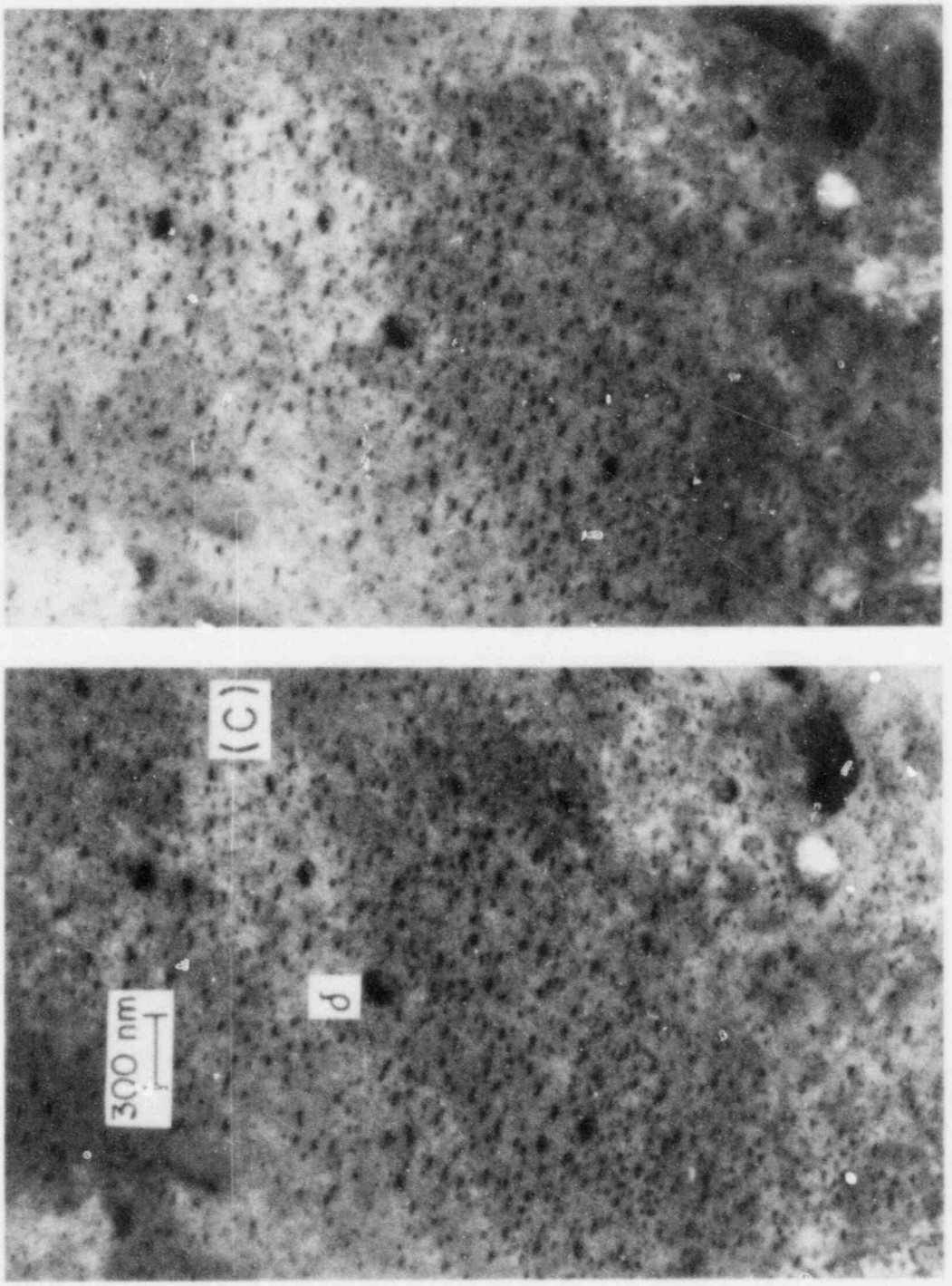


Fig. 2.2. (Contd.)

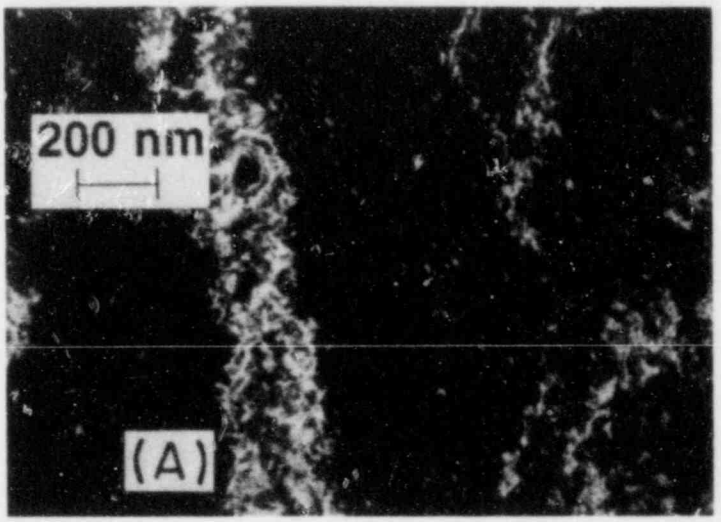


Fig. 2.3. TEM Micrographs Similar to Figs. 2.1 and 2.2 But from Tube $16^{5}$AG10. (A) Bright-field image; (B) indexed SAD pattern showing reflections from cubic $ZrO_2$ and δ hydride. Two different zones of the cubic $ZrO_2$ and three zones of the δ hydride are shown in (B).

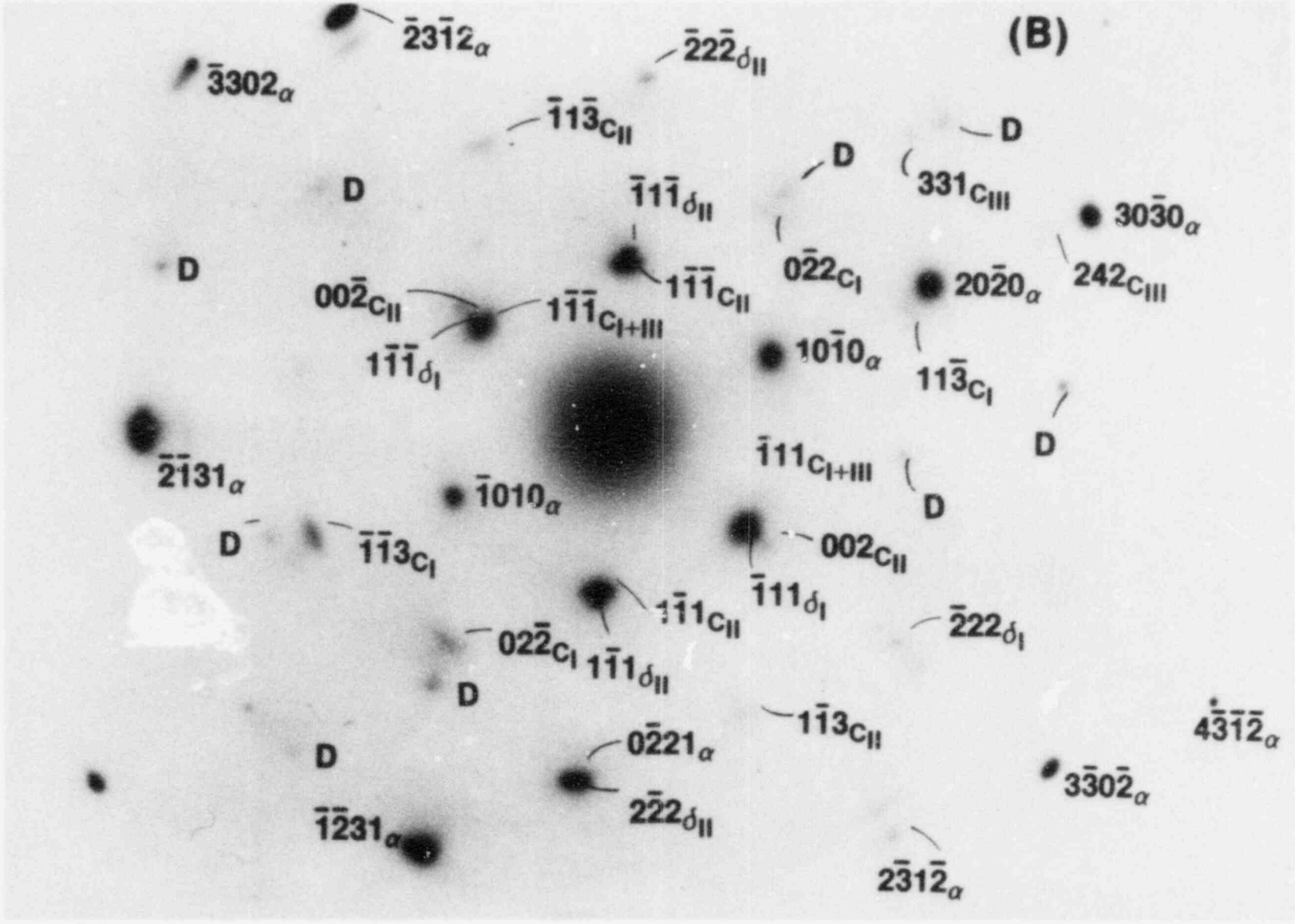
(B)
$\bar{2}3\bar{1}\bar{2}_{\alpha}$
$\bar{2}\bar{2}\bar{2}_{\delta_{II}}$
$\bar{3}302_{\alpha}$
$\bar{1}1\bar{3}_{C_{II}}$
D
D
D
$331_{C_{III}}$
$\bar{1}1\bar{1}_{\delta_{II}}$
$30\bar{3}0_{\alpha}$
D
$0\bar{2}2_{C_I}$
$20\bar{2}0_{\alpha}$
$242_{C_{III}}$
$00\bar{2}_{C_{II}}$
$1\bar{1}\bar{1}_{C_{II}}$
$1\bar{1}\bar{1}_{C_{I+III}}$
$1\bar{1}\bar{1}_{\delta_I}$
$10\bar{1}0_{\alpha}$
$11\bar{3}_{C_I}$
D
$\bar{2}\bar{1}31_{\alpha}$
$\bar{1}111_{C_{I+III}}$
$\bar{1}010_{\alpha}$
D
D
$\bar{1}\bar{1}3_{C_I}$
$002_{C_{II}}$
$\bar{1}111_{\delta_I}$
$1\bar{1}1_{C_{II}}$
$\bar{2}22_{\delta_I}$
$02\bar{2}_{C_I}$
$1\bar{1}1_{\delta_{II}}$
D
$1\bar{1}3_{C_{II}}$
$4\bar{3}\bar{1}\bar{2}_{\alpha}$
D
$0\bar{2}21_{\alpha}$
$3\bar{3}0\bar{2}_{\alpha}$
$2\bar{2}2_{\delta_{II}}$
$\bar{1}\bar{2}31_{\alpha}$
$2\bar{3}\bar{1}\bar{2}_{\alpha}$

Fig. 2.3. (Contd.)

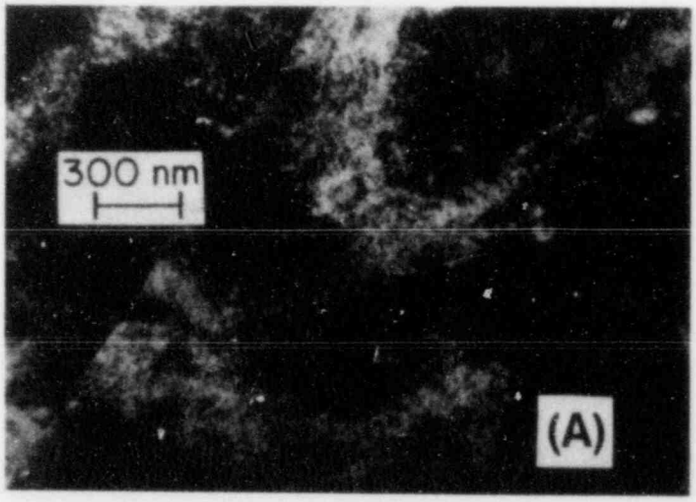


Fig. 2.4. TEM Micrographs from a Different Region of Cladding Tube 165AG10. (A) Bright-field image; (B) SAD pattern showing (110) zones of the cubic $ZrO_2$ and δ hydride and [$\bar{1}$102] zone axis of the α-Zr matrix.

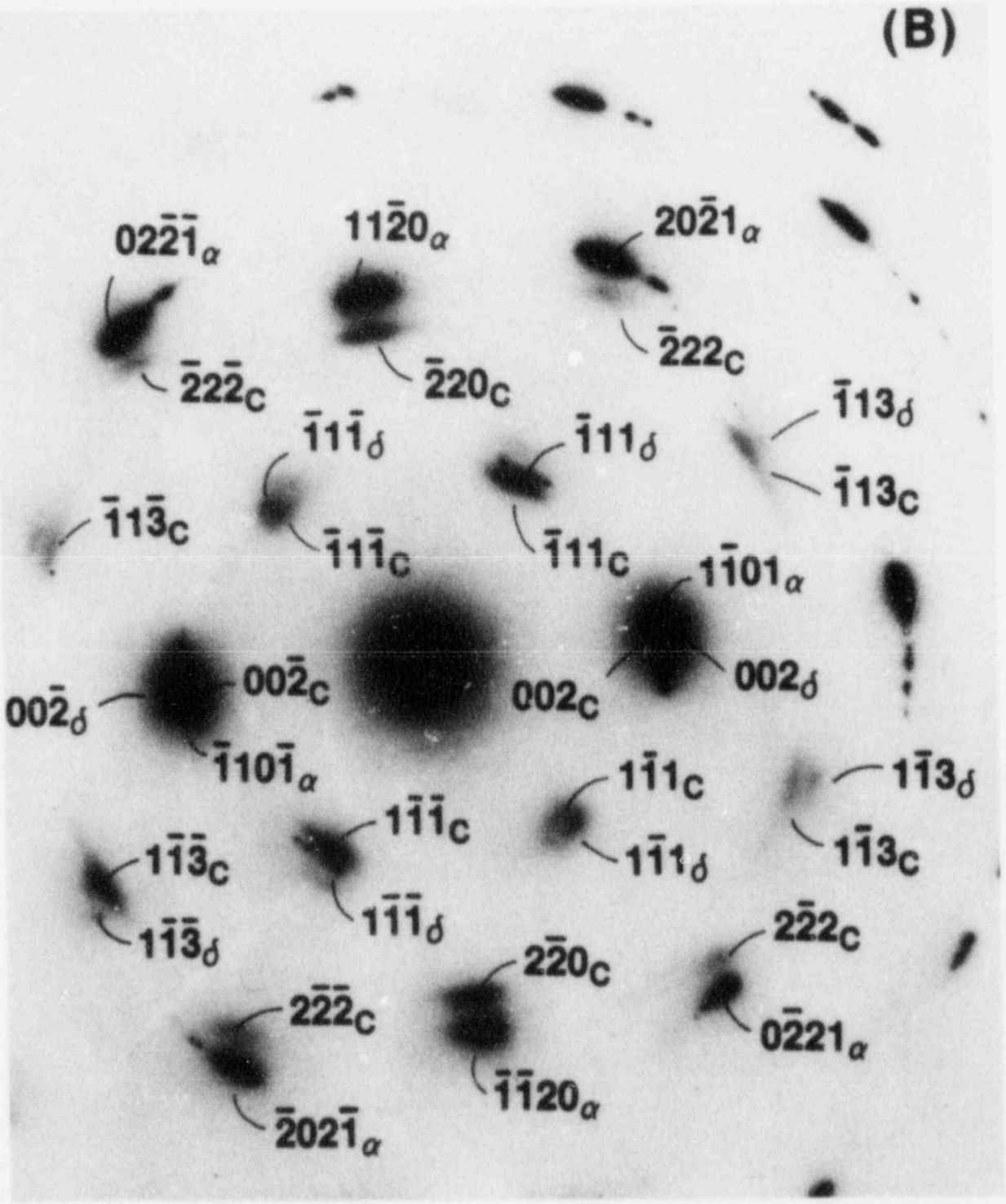
(B)
$02\bar{2}\bar{1}_\alpha$
$11\bar{2}0_\alpha$
$20\bar{2}1_\alpha$
$\bar{2}22_C$
$\bar{2}20_C$
$\bar{2}2\bar{2}_C$
$\bar{1}13_\delta$
$\bar{1}11_\delta$
$\bar{1}11_\delta$
$\bar{1}13_C$
$\bar{1}13_C$
$\bar{1}11_C$
$\bar{1}11_C$
$1\bar{1}01_\alpha$
$00\bar{2}_C$
$00\bar{2}_\delta$
$002_C$
$002_\delta$
$\bar{1}10\bar{1}_\alpha$
$1\bar{1}1_C$
$1\bar{1}3_\delta$
$1\bar{1}\bar{1}_C$
$1\bar{1}3_C$
$1\bar{1}3_C$
$1\bar{1}1_\delta$
$1\bar{1}3_C$
$1\bar{1}\bar{1}_\delta$
$1\bar{1}3_\delta$
$2\bar{2}2_C$
$2\bar{2}0_C$
$2\bar{2}\bar{2}_C$
$0\bar{2}21_\alpha$
$\bar{1}\bar{1}20_\alpha$
$\bar{2}02\bar{1}_\alpha$

Fig. 2.4. (Contd.)

Fig. 2.3(B) indicates two different zones of the δ-hydride and three zones of the cubic-$ZrO_2$ precipitates. As pointed out previously,[1] the δ hydrides shown in Figs. 2.1-2.4 are too small to be observed by SEM or optical microscopy.

## B. Radiation-induced Precipitation of Cubic $ZrO_2$ and $Zr_3O$ Particles by Electron Irradiation in the HVEM

### 1. Introduction

The $Zr_3O$[2] and cubic-$ZrO_2$ precipitates,[1] 2-6 and 5-10 nm in size, respectively (e.g., Figs. 2.1 and 2.2), in the irradiated cladding form via radiation-induced segregation and precipitation. The phenomenon of radiation-induced precipitation has been reported extensively for other alloy systems (e.g., see Ref. 3). Although the potential significance has not been recognized, circumstantial evidence reported in the literature suggests that the interaction between irradiation-induced defects and nonmetallic elements plays an important role in the deformation behavior of Zr-base alloys.[4-7] More recently, Loomis and Zaluzec[8] observed $Ti_3(O_{1-x}N_x)$ precipitates on dislocation substructures in a V-15Cr-5Ti alloy containing nonmetallic impurities after irradiation by 4-MeV Ni ions. To demonstrate precipitation of the $Zr_3O$ and cubic-$ZrO_2$ phases during in-situ irradiation at the test temperature, several TEM thin-foil specimens from tubes that exhibited brittle-fracture behavior were irradiated by 1-MeV electrons in the HVEM at 325°C in a vacuum of ~$1.3 \times 10^{-4}$ Pa.

### 2. Results

A thin-foil specimen obtained from a Zircaloy-4 cladding tube from the H. B. Robinson reactor was irradiated in the HVEM at 325°C. After irradiation by 1-MeV electrons for ~30 min, changes were observed in the bright-field image, as shown in Fig. 2.5(A). The changes are due to some kind of precipitation. Examination of the SAD pattern [Fig. 2.5(B)] showed reflections of cubic $ZrO_2$ as well as the superlattice reflections of the $Zr_3O$ phase. An SAD pattern taken from the same region at room temperature prior to the heating did not show reflections of either phase. Figure 2.5(C) shows the dark-field image obtained from the reflection containing the (0002) of the α-Zr matrix and $Zr_3O$ and the (002) of the cubic $ZrO_2$. Figure 2.5(D) shows the

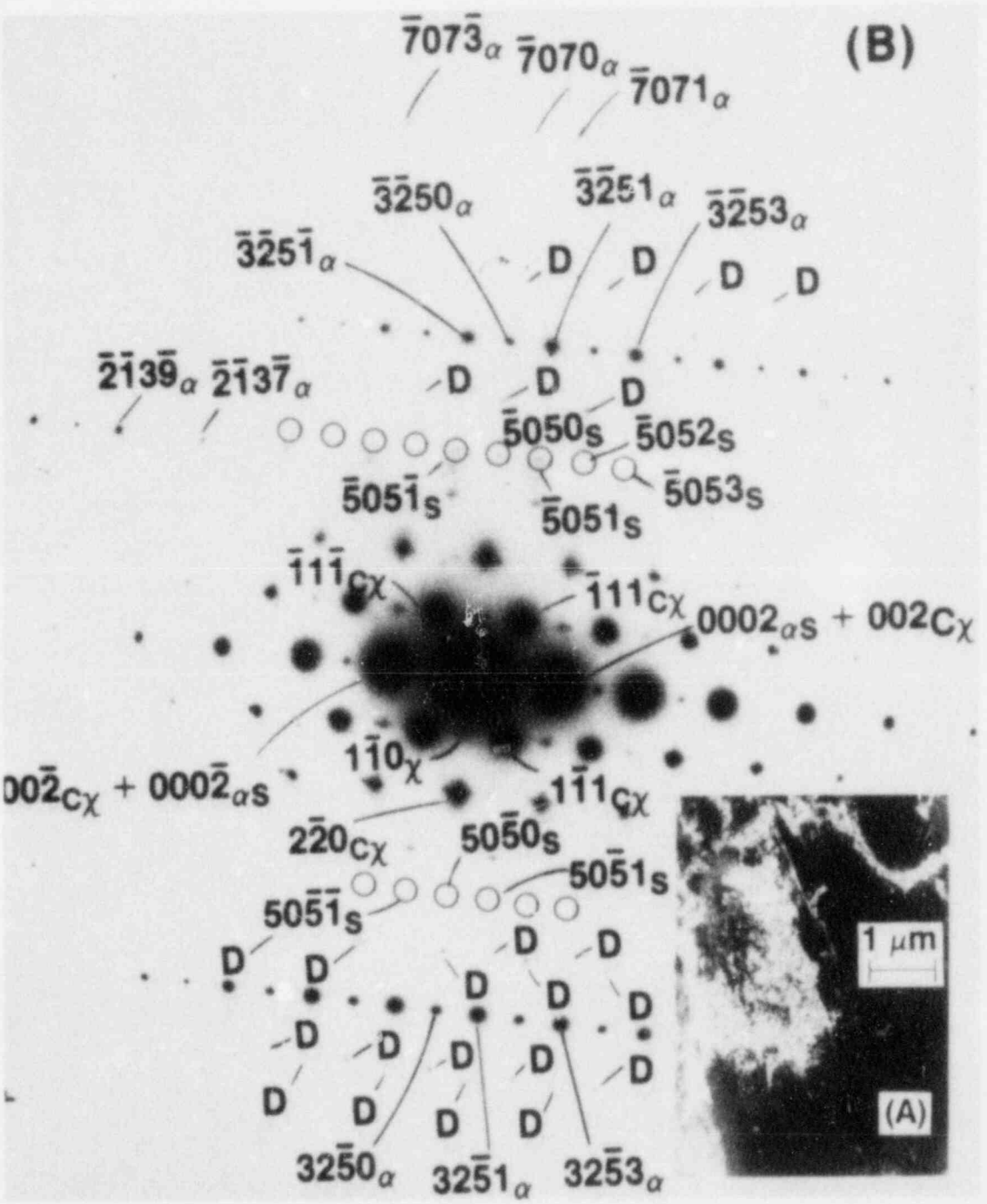


Fig. 2.5. HVEM Micrographs Obtained at Room Temperaure after 1-MeV Electron Irradiation of a Thin-Foil Specimen of H. B. Robinson Zircaloy-2 Cladding at 325°C in Vacuum. (A) Bright-field image; (B) indexed SAD pattern showing the (110) zone of the cubic $ZrO_2$ and superlattice reflections from the $Zr_3O$; (C) dark-field image from the reflections containing the (002) of the cubic $ZrO_2$ and (0002) of the $Zr_3O$ and α-Zr matrix; (D) dark-field image from the $(\bar{1}1\bar{1})$ of cubic $ZrO_2$.

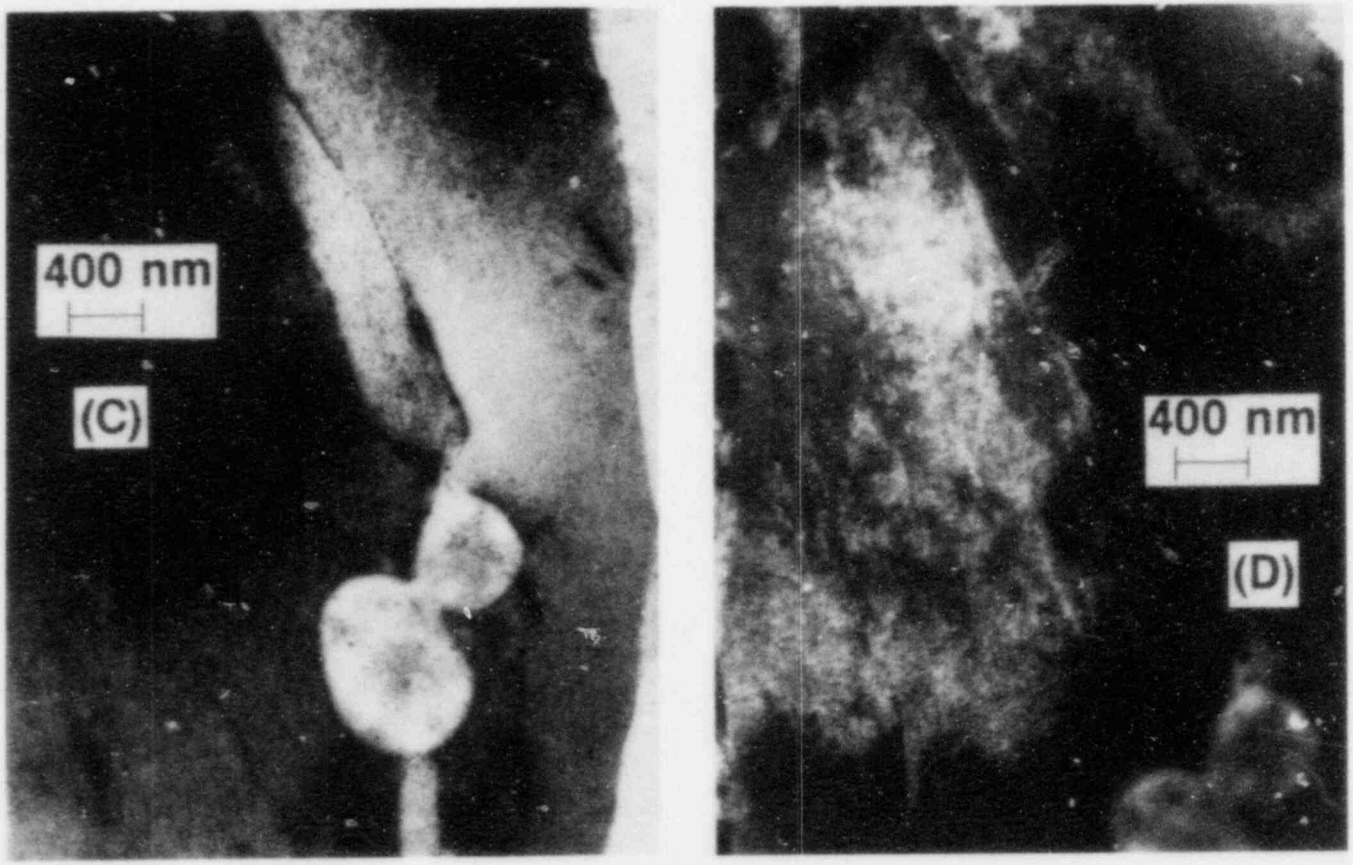


Fig. 2.5. (Contd.)

dark-field image of the $(\bar{1}1\bar{1})$ of cubic $ZrO_2$. Both figures show very fine particles of cubic $ZrO_2$ $\lesssim$10 nm in size. Bright- and dark-field images and an indexed SAD pattern similar to those of Fig. 2.5 are also shown in Fig. 2.6. In the SAD pattern of Fig. 2.6(B), superlattice reflections of the $Zr_3O$ are not visible.

The in-situ electron irradiation experiment demonstrates irradiation-induced precipitation of the cubic $ZrO_2$ and $Zr_3O$ in the H. B. Robinson Zircaloy-4 cladding material at 325°C. In contrast, neither precipitation nor dissolution of the δ hydride was observed during the HVEM irradiation at this temperature; thus, the δ-hydride phase was probably not formed by an irradiation-induced precipitation process.

## C. Procurement of Fuel Rods with In-Reactor PCI Defects

In this reporting period, several defueled Zircaloy-2 cladding sections were obtained which contain PCI or PCI-related defects that originated during actual reactor operation. The axial positions of the PCI defects in each cladding section were obtained from encircling-coil eddy current scans. Each fuel rod that showed a distinct peak in the eddy current scan was sectioned with an abrasive cut-off wheel such that the defect was located in the middle of the ~200-mm-long segment. The fuel was then removed from the tube by mechanical vibration and pressing.

In addition to the PCI-defected cladding sections, two metallographic specimens with PCI defects were obtained from the same source. The specimens were polished and etched to reveal the brittle cracks and hydride stringers.

A few Zircaloy-4 guide tube sections (~180 mm long) were also obtained. The guide tubes, which had not been exposed to fission product species, were discharged from an operating commercial power reactor after ~5 years of service. The annealed and recrystallized material was irradiated to an estimated fluence of ~8 x $10^{21}$ $n \cdot cm^{-2}$ ($E > 1$ MeV). Information on the materials is listed in Table 2.1. The specimens will be analyzed by SEM and

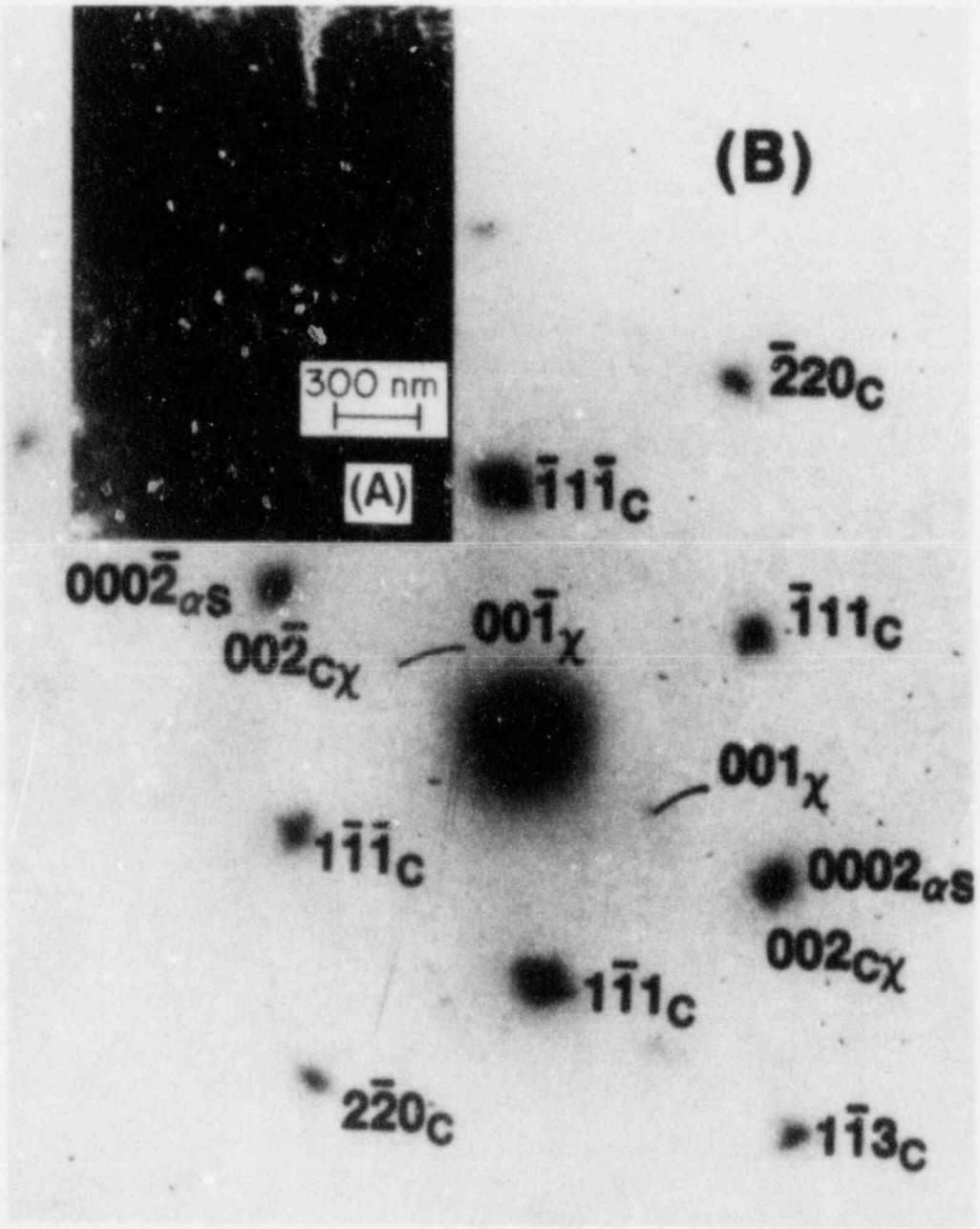


Fig. 2.6. HVEM Micrographs from a Different Region of the Specimen of Fig. 2.5.

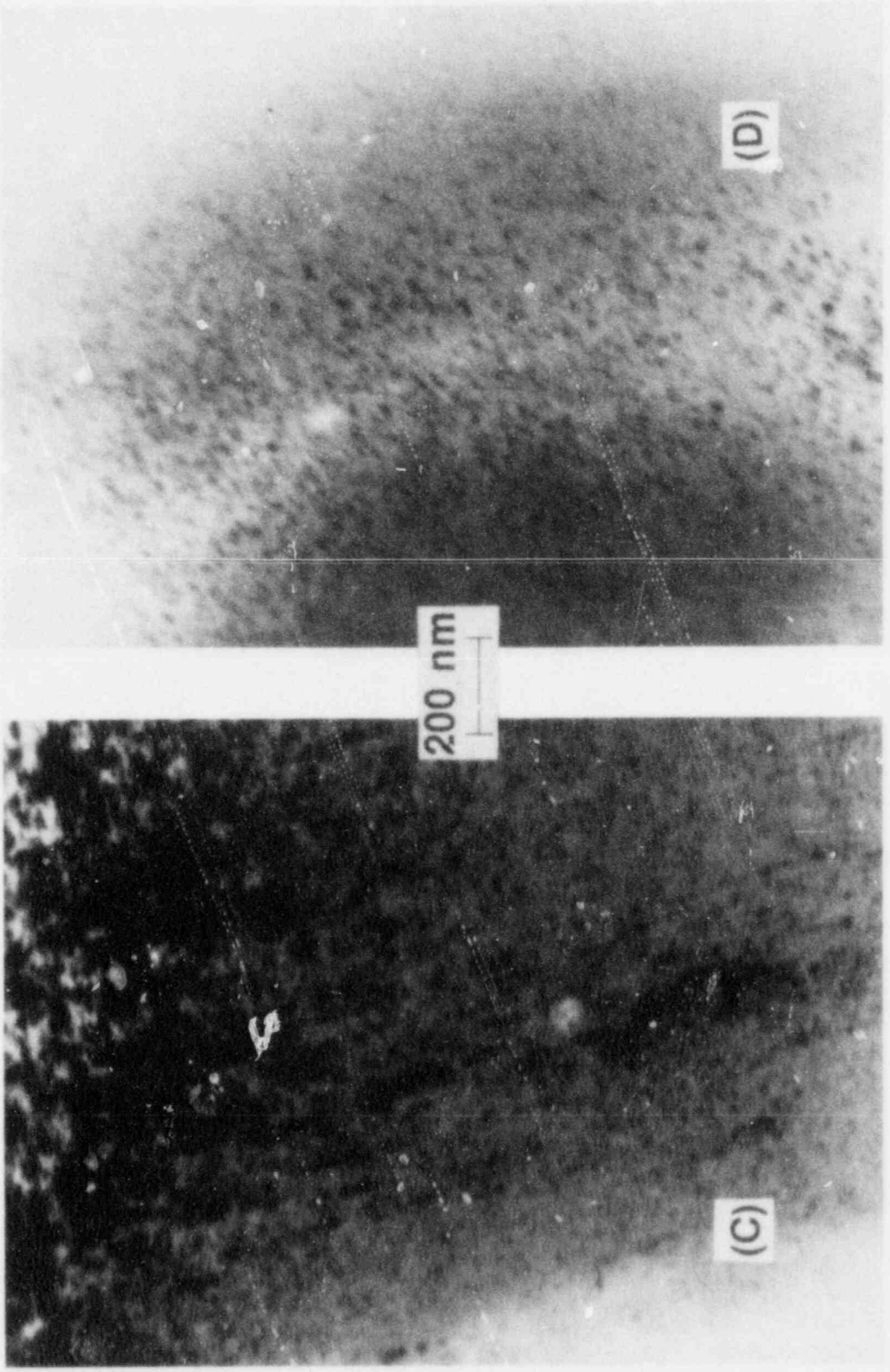


Fig. 2.6. (Contd.)

Table 2.1. Summary of Cladding Sections with PCI Defects and Irradiated Guide Tube Specimens for Microstructural Characterization

| Specimen Identification Number | Fuel Rod/Assembly Number | Axial Location[a] | Fuel |
|---|---|---|---|
| Defueled Cladding Sections | | | |
| SF1A | Rod SF1-00352 | 107.5-115.5 | $UO_2$-$Gd_2O_3$ fuel |
| BE4A | Rod BE4-3544 | 122-130 | $UO_2$ fuel |
| BE4B | Rod BE4-3544 | 130-138 | $UO_2$ fuel |
| GE1A | Rod GE1-00123 | 46-54 | $UO_2$-$Gd_2O_3$ fuel |
| GE1B | Rod GE1-00123 | 136-144 | $UO_2$-$Gd_2O_3$ fuel |
| Metallographic Sections | | | |
| MM-992 | Rod GE1-00123 | 58.75-59.25 | $UO_2$-$Gd_2O_3$ fuel |
| MM-99 | Rod GE1-00123 | 62.75-63.25 | $UO_2$-$Gd_2O_3$ fuel |
| Guide Tube Sections | | | |
| GT-3D | Assembly BT03 | Tube No. 3, Span 2-3[b] | -- |
| GT-1D | Assembly BT03 | Tube No. 1, Span 5-6 | -- |

[a]Inches from bottom of the rod.
[b]Fuel assembly grid span.

TEM-HVEM techniques to establish whether they have microstructural characteristics similar to those reported for cladding from the internal gas-pressurization and expanding-mandrel tests at 325°C. The structure-property relationships of the PCI-defected cladding and simulation-test specimens will be compared.

## D. References for Chapter II


1. H. M. Chung, in Light-Water-Reactor Safety Fuel Systems Research Programs: Quarterly Progress Report, July-September 1984, NUREG/CR-3980 Vol. III, ANL-84-61 Vol. III (April 1985), pp. 20-39.

2. H. M. Chung, "TEM-HVEM Observation of Ordered Zirconium-Oxygen Phase in Zircaloy Spent-Fuel Cladding," pp. 297-333 in Proc. Intl. Symp. on Environmental Degradation of Materials in Nuclear Power Systems - Water Reactors, Myrtle Beach, SC, August 22-24, 1983.

3. F. V. Nolfi, ed., Phase Transformation During Irradiation, Elsevier Science Publishing Co. (1983).

4. K. Veevers and W. B. Rotsey, J. Nucl. Mater. 27, 108 (1968).

5. D. Lee and E. F. Koch, J. Nucl. Mater. 50, 162 (1974).

6. A. Jostsons, P. M. Kelly, R. G. Blake, and K. Farrell, pp. 46-61 in Effects of Radiation on Structural Materials, ASTM STP 683, J. A. Sprague and D. Kramer, eds., American Society for Testing and Materials (1979).

7. R. H. Zee, A. Rogerson, G. J. C. Carpenter, and J. Watters, J. Nucl. Mater. 120, 223 (1984).

8. B. A. Loomis and N. J. Zaluzec, First Intl. Conf. on Fusion Reactor Materials, December 3-6, 1984, Tokyo, Japan; Program and Collected Abstracts booklet, Abstract 6P-21, p. 235.

Distribution for NUREG/CR-3980 Vol. IV (ANL-84-61 Vol. IV)

Internal:

R. Avery
O. K. Chopra
H. M. Chung
L. W. Deitrich
C. E. Dickerman
G. R. Fenske
F. Y. Fradin
B. R. T. Frost
E. E. Gruber
G. L. Hofman
M. Ishii
W. D. Jackson
C. E. Johnson
T. F. Kassner (10)
K. L. Kliewer
J. M. Kramer
D. S. Kupperman
D. J. Lam
Y. Y. Liu
P. A. Lottes
P. S. Maiya
K. Natesan
L. A. Neimark
F. A. Nichols
P. R. Okamoto
R. G. Palm
J. Y. Park
R. B. Poeppel
L. E. Rehn
J. Rest (10)
W. E. Ruther
R. A. Scharping
W. J. Shack (3)
E. M. Stefanski (2)
R. V. Strain
C. E. Till
H. C. Tsai
R. A. Valentin
A. Villalobos
R. W. Weeks
H. Wiedersich
F. L. Yaggee
ANL Patent Dept.
ANL Contract File
ANL Libraries (3)
TIS Files (6)

External:

NRC, for distribution per R3 (275)
DOE-TIC (2)
Manager, Chicago Operations Office, DOE
R. Tom, DOE-CH
Materials Science and Technology Division Review Committee:
C. B. Alcock, U. Toronto
A. Arrott, Simon Fraser U.
R. C. Dynes, Bell Labs., Murray Hill
A. G. Evans, U. California, Berkeley
H. K. Forsen, Bechtel National, Inc., San Francisco
E. Kay, IBM San Jose Research Lab.
M. B. Maple, U. California, San Diego
P. G. Shewmon, Ohio State U.
J. K. Tien, Columbia U.
J. W. Wilkins, Cornell U.
R. B. Adamson, General Electric Co., Vallecitos Nuclear Center, P. O. Box 460, Pleasanton, Calif. 94566
P. L. Andresen, General Electric Corporate Research and Development, Schenectady, N. Y. 12301
G. A. Arlotto, Office of Nuclear Regulatory Research, USNRC, Washington
D. Atteridge, Battelle Pacific Northwest Lab., P. O. Box 999, Richland, Wash. 99352
D. L. Burman, Westinghouse PWR Systems Div., P. O. Box 355, Pittsburgh, Pa. 15230
L. K. Chan, Office of Nuclear Regulatory Research, USNRC, Washington
B. Cox, Chalk River Nuclear Labs., AECL, Chalk River, Ont., K0J 1J0, Canada
R. B. Foulds, Office of Nuclear Reactor Regulation, USNRC, Washington
S. M. Gehl, Electric Power Research Inst., P. O. Box 10412, Palo Alto, Calif. 94304
J. H. Gittus, Springfields Nuclear Power Development Labs., U. K. Atomic Energy Authority, Springfields, Salwick, Preston, PR4 ORR, England
R. R. Hobbins, EG&G/INEL, 1520 Sawtelle Dr., Idaho Falls, Idaho 83401
W. V. Johnston, Office of Nuclear Reactor Regulation, USNRC, Washington
R. L. Jones, Electric Power Research Inst., P. O. Box 10412, Palo Alto, Calif. 94304
K. R. Jordan, Nuclear Fuel Div., Monroeville Nuclear Center, Westinghouse Electric Corp., Monroeville, Pa. 15146
C. N. Kelber, Office of Nuclear Regulatory Research, USNRC, Washington

E. Kohn, Atomic Energy of Canada Ltd., Sheridan Park Research Community, Mississauga, Ont., Canada L5K 1B2
P. M. Lang, Office of Converter Reactor Deployment, USDOE, Washington, D. C. 20545
D. D. Lanning, Battelle Pacific Northwest Lab., P. O. Box 999, Richland, Wash. 99352
R. A. Lorenz, Oak Ridge National Lab., P. O. Box X, Oak Ridge, Tenn. 37830
P. MacDonald, EG&G/INEL, 1520 Sawtelle Dr., Idaho Falls, Idaho 83401
G. P. Marino, Office of Nuclear Regulatory Research, USNRC, Washington
S. McDonald, Westinghouse Electric Corp., R&D Center, Beulah Rd., Pittsburgh, Pa. 15235
K. R. Merckx, Exxon Nuclear, Inc., 2955 George Washington Way, Richland, Wash. 99352
A. C. Millunzi, Office of Nuclear Energy, USDOE, Washington, D. C. 20545
D. R. O'Boyle, Commonwealth Edison Co., P. O. Box 767, Chicago, Ill. 60690
R. N. Oehlberg, Electric Power Research Inst., P. O. Box 10412, Palo Alto, Calif. 94304
M. F. Osborne, Oak Ridge National Lab., P. O. Box X, Oak Ridge, Tenn. 37830
D. E. Owen, EG&G Idaho, P. O. Box 88, Middletown, Pa. 17057
T. P. Papazoglou, Lynchburg Research Center, Babcock & Wilcox Co., P. O. Box 1260, Lynchburg, Va. 24505
J. T. A. Roberts, Electric Power Research Inst., P. O. Box 10412, Palo Alto, Calif. 94304
H. H. Scott, Office of Nuclear Regulatory Research, USNRC, Washington
R. D. Silver, Office of Nuclear Reactor Regulation, USNRC, Washington
P. Smerd, Combustion Engineering, Inc., P. O. Box 500, Windsor, Conn. 06095
A. A. Solomon, School of Nuclear Engineering, Purdue U., West Lafayette, Ind. 47907
R. Van Houten, Office of Nuclear Regulatory Research, USNRC, Washington

NRC FORM 335 (2-84) NRCM 1102, 3201, 3202

U.S. NUCLEAR REGULATORY COMMISSION

## BIBLIOGRAPHIC DATA SHEET

SEE INSTRUCTIONS ON THE REVERSE

1 REPORT NUMBER (Assigned by TIDC add Vol. No., if any)

NUREG/CR-3980 Vol. IV
ANL-85-61 Vol. IV

2 TITLE AND SUBTITLE

Light-Water-Reactor Safety Fuel Systems Research Programs: Quarterly Progress Report, October-December 1984

3 LEAVE BLANK

4 DATE REPORT COMPLETED

| MONTH | YEAR |
|---|---|
| July | 1985 |

5 AUTHOR(S)

J. Rest and H. M. Chung

6 DATE REPORT ISSUED

| MONTH | YEAR |
|---|---|
| August | 1985 |

7 PERFORMING ORGANIZATION NAME AND MAILING ADDRESS (Include Zip Code)

Argonne National Laboratory
9700 South Cass Avenue
Argonne, Illinois 60439

8 PROJECT/TASK/WORK UNIT NUMBER

9 FIN OR GRANT NUMBER

A2016, A2017

10 SPONSORING ORGANIZATION NAME AND MAILING ADDRESS (Include Zip Code)

Division of Accident Evaluation
Office of Nuclear Regulatory Research
U. S. Nuclear Regulatory Commission
Washington, D. C. 20555

11a TYPE OF REPORT

Technical

b PERIOD COVERED (Inclusive dates)

October-December 1984

12 SUPPLEMENTARY NOTES

13 ABSTRACT (200 words or less)

This progress report summarizes the Argonne National Laboratory work performed during October, November, and December 1984 on water reactor safety problems related to fuel and fuel cladding materials. The research and development areas covered are Transient Fuel Response and Fission Product Release and Clad Properties for Code Verification.

14 DOCUMENT ANALYSIS - a KEYWORDS/DESCRIPTORS

fission product modeling
fission product release
irradiated Zircaloy cladding
mandrel loading tests
Zircaloy fracture
$Zr_3O$ precipitation

b IDENTIFIERS/OPEN-ENDED TERMS

15 AVAILABILITY STATEMENT

Unlimited

16 SECURITY CLASSIFICATION

(This page)
Unclassified

(This report)
Unclassified

17 NUMBER OF PAGES

62

18 PRICE